

Fate of Pyroxenite-derived Melts in the Peridotitic Mantle: Thermodynamic and Experimental Constraints

S. LAMBART^{1,2*}, D. LAPORTE^{1,2}, A. PROVOST^{1,2} AND P. SCHIANO^{1,2}

¹LABORATOIRE MAGMAS ET VOLCANS, CLERMONT UNIVERSITÉ, UNIVERSITÉ BLAISE PASCAL, BP 10448, 63000 CLERMONT-FERRAND, FRANCE

²CNRS, UMR 6524, IRD, R 163, 5 RUE KESSLER, F-63038 CLERMONT-FERRAND CEDEX, FRANCE

RECEIVED FEBRUARY 7, 2011; ACCEPTED NOVEMBER 16, 2011
ADVANCE ACCESS PUBLICATION JANUARY 23, 2012

We performed a thermodynamic and experimental study to investigate the fate of pyroxenite-derived melts during their migration through the peridotitic mantle. We used a simplified model of interaction in which peridotite is impregnated by and then equilibrated with a finite amount of pyroxenite-derived liquid. We considered two pyroxenite compositions and three contexts of pyroxenitic melt impregnation: (1) in a subsolidus lithospheric mantle; (2) beneath a mid-ocean ridge (MOR) in a subsolidus asthenospheric mantle at high pressure; (3) beneath a MOR in a partially molten asthenospheric mantle. Calculations were performed with *pMELTS* at constant pressure and temperature with a melt–rock ratio varying in the range 0–1. Concurrently, a series of impregnation experiments was performed at 1 and 1.5 GPa to reproduce the final stages of the calculations where the melt–rock ratio is 1. Incoming melt and host-rocks react differently according to the melt composition and the physical state of the surrounding mantle. Whereas clinopyroxene (Cpx) is systematically a reaction product, the role of olivine (Ol) and orthopyroxene (Opx) depends on the incoming melt silica activity a_{SiO_2} : if it is lower than the silica activity $a_{\text{SiO}_2}^0$ of a melt saturated in Ol and Opx at the same pressure *P* and temperature *T*, Opx is dissolved and Ol precipitates, and conversely if $a_{\text{SiO}_2} > a_{\text{SiO}_2}^0$. Such contrasted reactions between pyroxenitic melts and peridotitic mantle may generate a large range of new lithological heterogeneities (wehrlite, websterite, clinopyroxenite) in the upper mantle. Also, our study shows that the ability of pyroxenite-derived melts to migrate through the mantle depends on the melting degree of the surrounding peridotite. The reaction of these melts with a subsolidus mantle results in strong melt consumption (40–100%) and substantial Cpx production (with some spinel or garnet, depending on *P*). This is expected

to drastically decrease the system permeability and the capacity of pyroxenite-derived melts to infiltrate neighbouring rocks. In contrast, melt migration to the surface should be possible if the surrounding mantle is partially melted; although liquid reactivity varies with composition, melt consumption is restricted to less than 20%. Hence, magma–rock interactions can have a significant impact on the dynamics of melting and magma migration and should not be neglected when modelling the partial melting of heterogeneous mantle.

KEY WORDS: experimental petrology; melt–peridotite interactions; MORB genesis; *pMELTS*; pyroxenite

INTRODUCTION

The upper mantle is likely to contain a significant fraction of pyroxenite: 2–5% according to Hirschmann & Stolper (1996), based on the proportion in orogenic peridotite massifs. Mantle pyroxenites show a large spectrum of bulk-rock compositions and modal proportions, presumably reflecting different origins [crystallization of asthenospheric melts percolating through the lithospheric mantle (Shervais *et al.*, 1973); *in situ* formation by metamorphic differentiation (Dick & Sinton, 1979); recycling of subducted oceanic crust into the asthenosphere (Polvé & Allègre, 1980); among others] and different degrees of interaction and re-equilibration with the surrounding peridotites. Whatever their origin, pyroxenites may play an important

*Corresponding author. Present address: California Institute of Technology, MC 170-25, Pasadena, CA 91125, USA. Telephone: +1 626 240 9705. Fax: +1 626 568 0935. E-mail: slambart@caltech.edu

© The Author 2012. Published by Oxford University Press. All rights reserved. For Permissions, please e-mail: journals.permissions@oup.com

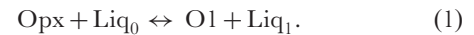
role in controlling the chemical variability of mantle-derived melts (Sleep, 1984; Allègre & Turcotte, 1986; Sobolev *et al.*, 2007).

The role of pyroxenite lithologies in oceanic basalt generation has been studied in numerous geochemical (e.g. Le Roux *et al.*, 2002; Sobolev *et al.*, 2007) and experimental (e.g. Kogiso *et al.*, 2004a, and references therein) studies. Even if the fraction of pyroxenite in the upper mantle is small in comparison with peridotite, pyroxenites may indeed contribute to a significant proportion of the total melt production owing to their lower solidus temperatures and higher melt productivities (e.g. Hirschmann & Stolper, 1996; Pertermann & Hirschmann, 2003; Lambart *et al.*, 2009a). To fully describe partial melting processes in heterogeneous mantle, it is, however, necessary to take into account the interactions between the pyroxenites and/or pyroxenite-derived melts and the surrounding peridotite, which might have a significant role in melt extraction dynamics and, ultimately, in the preservation of a pyroxenite signature in aggregated melts erupted at the Earth's surface.

Pyroxenite–peridotite interaction processes depend on many chemical and physical parameters such as the size of the pyroxenite bodies (Kogiso *et al.*, 2004b), the composition of the pyroxenites and pyroxenite-derived melts (e.g. Morgan & Liang, 2005), and the nature of the transport mechanism (pervasive porous flow, focused flow in dunite channels or magma transport in dikes). Accordingly, these processes are very difficult to model or simulate in the laboratory. A few experimental studies have been carried out to better understand the chemical interactions between silicate melts and host peridotite. Morgan & Liang (2003, 2005) performed kinetic experiments on interactions between basaltic melt and peridotite, and observed more or less significant modifications of the peridotite assemblage as a function of melt composition. In this type of disequilibrium experiment, however, it is difficult to quantify the reactions involved and their impact on melt and peridotite composition. Yaxley & Green (1998) and Pilet *et al.* (2008) performed ‘sandwich’ experiments, in which a layer of material with a low solidus temperature was packed between layers of peridotite. Yaxley & Green (1998) used a mid-ocean ridge basalt (MORB)-type eclogite (GAl) and performed their experiments at 3.5 GPa, whereas Pilet *et al.* (2008) used a hornblende (AG4) at 1.5 GPa. Unlike Morgan & Liang's (2003, 2005) experiments, most of these experiments were run below the solidus temperature of peridotite, and so simulated the case of a partially molten pyroxenite body within a subsolidus peridotite host. These two studies led to opposite results: melts from GAl were consumed to produce orthopyroxene (Opx) whereas melts from AG4 dissolved Opx from the surrounding peridotite and precipitated olivine (Ol). Yaxley & Green's (1998) and Pilet *et al.*'s (2008) studies

deal chiefly with the effect of melt–rock reaction on melt composition, but a comparison of their results underlines the importance of the initial conditions (pressure and composition) for the reaction and shows that magma–rock interactions may have a significant impact on the lithological diversity of the mantle. A natural example is provided by pyroxenites from the Ronda Massif (SW Spain): according to Garrido & Bodinier (1999), some of these were produced by interaction between pyroxenite-derived alkali basalt melt and peridotite.

A major aspect of the interaction of pyroxenite-derived melts with host peridotite is the coupled dissolution of Opx and precipitation of Ol (or vice versa). This can be described by a simple reaction such as



In the case of a simple system at constant pressure and temperature, in which liquid, Ol and Opx are the only phases present, thermodynamic (Kelemen, 1990) and experimental (Daines & Kohlstedt, 1994) studies have shown that the mass ratio of precipitated Ol to dissolved Opx, $M_{\text{Ol}}/M_{\text{Opx}}$, is ~ 0.7 . Hence, Opx dissolution and Ol precipitation increase the proportion of melt in the system and facilitate its transport by increasing the porosity and permeability of mantle rocks. Inversely, Opx crystallization at the expense of Ol leads to a reduction of porosity and may slow down or even stop magma ascent by porous flow. This case highlights that basalt–peridotite interactions could significantly affect the rate of transport of magmas from their source region to the surface.

In this study, we try to evaluate the fate of melts from pyroxenitic sources during their transport through the peridotite mantle as functions of their composition, P – T conditions and the physical state (subsolidus vs partially molten) of the surrounding mantle. Three cases are considered in order to discuss the impact of melt–rock interactions on the chemical composition of melts, the chemical and mineralogical compositions of the surrounding peridotite, and the ability of the melts to infiltrate the surrounding rock.

- (1) Partial melting of pyroxenites in a subsolidus lithospheric mantle. If heterogeneous lithospheric mantle is affected by a temperature increase (for example, in the context of asthenospheric upwelling and lithospheric extension), pyroxenites—with lower solidus temperatures than peridotite (e.g. Hirschmann & Stolper, 1996)—will melt first and pyroxenite-derived melts will tend to infiltrate and react with the surrounding peridotite. Here, we want to test whether peridotite impregnation by a pyroxenitic melt can produce a new generation of pyroxenites with specific features and so increase the ‘lithodiversity’ of the mantle, as suggested by Garrido & Bodinier (1999).

- (2) Partial melting of pyroxenites in MORB-source mantle at high P (2.5 GPa). During mantle upwelling beneath mid-ocean ridges (MOR), pyroxenites start to melt at greater depths than peridotite owing to their lower solidus temperature. Here, our main objective is to determine whether the chemical exchange between the pyroxenites and subsolidus peridotite favour melt transport over relatively long distances or else lead to the isolation of partially molten pyroxenite bodies in unmolten peridotite.
- (3) Partial melting of pyroxenites in the MORB-source mantle at low P (1 GPa). At low pressure beneath MORs, both pyroxenites and peridotite will be partially molten. In a previous experimental study (Lambart *et al.*, 2009a), we showed that melts from pyroxenites and peridotites have similar major element compositions at 1–1.5 GPa, and so we predicted minimal interactions between pyroxenite-derived melts and the surrounding mantle and the preservation of a pyroxenite chemical signature during melt transport to the Earth's surface. Our purpose here is to test this hypothesis.

To model these three cases, we used a simplified model of interaction in which peridotite is impregnated by a finite amount of pyroxenite-derived melt. We used the thermodynamic model pMELTS (Ghiorso *et al.*, 2002) and the Adiabatic front end (Smith & Asimow, 2005) to compute the proportions and compositions of solid and liquid phases in the impregnated peridotite after chemical re-equilibration, as a function of the composition and amount of pyroxenite-derived melt. Concurrently, we carried out impregnation experiments in a piston-cylinder apparatus to test the validity of the calculations. The thermodynamic and experimental approaches, the main results and their implications for the chemical and mineralogical evolution of pyroxenite-derived melts and peridotites within the upper mantle are presented below.

THERMODYNAMIC AND EXPERIMENTAL STRATEGY

Peridotite–pyroxenite interaction model

Impregnation model

We consider a heterogeneous mantle composed of pyroxenite bodies dispersed in a peridotite matrix. In our calculations and experiments, peridotite–pyroxenite interactions are envisaged to occur in two stages: (1) impregnation of peridotite by a finite amount of pyroxenite-derived melt; (2) chemical re-equilibration of the impregnated peridotite at constant P and T . Input parameters are the composition of the pyroxenite-derived melt and the melt–rock ratio (i.e. the mass ratio of pyroxenite-derived melt to peridotite), which varies in the range 0–1. Output parameters

are the proportions and compositions of each phase in the impregnated peridotite after re-equilibration.

Starting peridotite and pyroxenite compositions

For the peridotite end-member, we chose a spinel lherzolite from Mont Briançon, French Massif Central (Bri2; Table 1). In terms of major-element composition this sample is intermediate between fertile mantle MM3 of Baker & Stolper (1994) and depleted mantle DMM1 of Wasylenki *et al.* (2003). Two pyroxenites from the Beni Bousera ultramafic massif (northern Morocco) were used in both calculations and experiments: M5-40 and M7-16 (Table 1). The criteria used to select these two samples were discussed by Lambart *et al.* (2009a). M5-40 is a garnet (Gt) websterite, close to the mean composition of the natural pyroxenite population. M7-16 has a more extreme composition, with low SiO₂ and high FeO contents (43.6 and 14.5%, respectively; unless otherwise stated, all percentages in this paper—oxide concentrations, phase proportions, norms, etc.—are reported by weight). Both pyroxenites are olivine normative, but they show different degrees of silica undersaturation: M7-16 is nepheline (Ne) normative (2.3%) and M5-40 is hypersthene (Hy) normative (8.3%).

P–T conditions

We consider that the pyroxenite-derived melt reacts with the surrounding peridotite at the P – T conditions of its formation and that impregnation takes place at constant P – T . To model the partial melting of pyroxenites in a subsolidus lithospheric mantle (case 1), we considered melts formed at 1250°C and 1.5 GPa. These conditions correspond to a subcontinental lithospheric mantle undergoing a thermal event owing to asthenospheric upwelling, such as the Ronda massif, SW Spain (Lenoir *et al.*, 2001). To model peridotite–pyroxenite interactions in MORB mantle sources (cases 2 and 3), we assumed that the heterogeneous mantle follows an adiabatic decompression path with a potential temperature of 1350°C; that is, close to the mean potential temperature beneath MORs according to Herzberg *et al.* (2007). Using the parameterization of McKenzie & O'Nions (1991), we selected two P – T couples lying on or close to this adiabatic decompression path: $P = 2.5$ GPa and $T = 1400$ °C to simulate the case where pyroxenites M5-40 and M7-16 are partially molten whereas peridotite Bri2 is subsolidus (case 2); $P = 1$ GPa and $T = 1290$ °C to simulate the case where both pyroxenites and peridotite are partially molten (case 3). The compositions of the partial melts of pyroxenites M7-16 and M5-40 at 1250°C and 1.5 GPa, and 1290°C and 1 GPa were determined by Lambart *et al.* (2009a) and are given in Table 2. The degree of melting is close to 10% in both pyroxenites at 1250°C and 1.5 GPa, and close or equal to 100% at 1290°C and 1 GPa. As discussed below, we performed two new experiments to determine the composition

Table 1: Peridotites Bri2, MM3 and DMM1 and pyroxenites M5-40 and M7-16, compared with the mean composition of group-A pyroxenites from Ronda Massif (SW Spain; Garrido & Bodinier, 1999)

	Bri2	M5-40	M7-16	Group A	MM3	DMM1
SiO ₂	45.1	48.53	43.58	47.1	45.5	44.9
TiO ₂	0.08	0.52	0.75	0.51	0.11	0.04
Al ₂ O ₃	2.7	12.37	13.73	13.79	3.98	2.38
Cr ₂ O ₃	0.27	0.12	0.07	—	0.68	0.39
FeO	7.6	9.02	14.51	9.76	7.18	8.34
MnO	0.12	0.20	0.30	0.20	0.13	0.13
MgO	41.8	16.64	12.52	14.05	38.3	41.59
CaO	2.2	10.89	13.77	11.91	3.57	2.14
Na ₂ O	0.19	1.65	0.75	1.32	0.31	0.055
K ₂ O	0.00	0.06	0.03	0.02	—	0.006
Mg-no.	90.7	76.7	60.6	72.0	90.5	89.9
Ne/Ol/Hy/	0/69.6/18.6/	0/27.7/8.3/	2.3/31.7/0/	0/24.4/8.6/	0/62.5/18.8/	0/69.2/20.5/
Di/Fds*	3.5/8.1	22.4/40.5	28.2/36.3	22.5/43.5	6.6/12.1	3.5/6.8

Bri2 is a spinel lherzolite from Mont Brianon, French Massif Central; M5-40 and M7-16 are pyroxenites from Beni Bousera ultramafic massif (Morocco). Bri2 was analysed by inductively coupled plasma atomic emission spectrometry (ICP-AES) at the Service d'Analyses des Roches et Minéraux (CRPG, Nancy, France); the K₂O content in Bri2 is <100 ppm. M5-40 and M7-16 were analysed by ICP-AES at Laboratoire Magmas et Volcans. MM3 is from Baker & Stolper (1994). DMM1 is from Wasylenki *et al.* (2003). Mg-number is the molar ratio $100 \text{ Mg}^{2+}/(\text{Mg}^{2+} + \text{Fe}^{2+})$; we considered that all iron was as Fe²⁺.

*CIPW norms: nepheline (Ne)/olivine (Ol)/hypersthene (Hy)/diopside (Di)/anorthite + albite + orthoclase (Fds).

of partial melts in pyroxenites M5-40 and M7-16 at 2.5 GPa and 1400°C; under these conditions, the degree of melting is 5% in M5-40 and 22% in M7-16 (Table 2).

Thermodynamic approach

The impregnation process is simulated at constant P and T by adding up to 100 g of pyroxenite-derived melt, in increments of 5 g, to 100 g of peridotite. At each step, we computed the chemical composition of the impregnated peridotite and we used the thermodynamic model pMELTS (Ghiorso *et al.*, 2002) to compute the equilibrium assemblage (phase compositions and proportions). From the evolution of phase proportions with increasing amount of added melt, we determined the modal reactions of impregnation using a method similar to that used by Baker & Stolper (1994) to compute melting reactions (see 'Thermodynamic results').

The software package pMELTS was initially developed to model liquid–solid and solid–solid phase relations in peridotitic systems. The fundamental problem solved by pMELTS is to calculate an equilibrium assemblage of phases by minimizing an appropriate potential energy, subject to constraints on bulk composition, temperature, pressure or volume, enthalpy or entropy, and optionally on oxygen fugacity f_{O_2} . It is calibrated in the system

SiO₂–TiO₂–Al₂O₃–Fe₂O₃–Cr₂O₃–FeO–MgO–CaO–Na₂O–K₂O–P₂O₅–H₂O, between 1 and 4 GPa. The interface Adibat-lph (Smith & Asimow, 2005) allows an automation of pMELTS calculations. In particular, we used the 'ADIABATASSIMILATE' variable of this interface to simulate the impregnation process, as it allows us to add a fixed mass of a second bulk composition after each calculation stage.

Below, we list the choices and constraints that we used in our thermodynamic study so that our calculations can be reproduced exactly.

- (1) To simulate the impregnation of peridotite by 0–100 g of melt, we used 21 steps, starting from 100 g of pure peridotite and adding 5 g of melt at each step.
- (2) Calculations were made at $f_{\text{O}_2} = \text{FMQ} - 1$ (i.e. the fayalite–magnetite–quartz buffer minus one log unit), close to the oxygen fugacity in our experiments (Laporte *et al.*, 2004) and to the oxygen fugacity in the mantle source of MORB (Christie *et al.*, 1986; Cottrell & Kelley, 2011). For comparison, we also performed some calculations at FMQ and FMQ – 2 and we obtained very similar results.
- (3) Of the two garnet models (from Berman & Koziol, 1991) available in pMELTS, we used the older, uncorrected one, which is the default in Adibat.lph. This

Table 2: Compositions (wt %) of pyroxenite-derived and peridotite-derived melts used in the impregnation models

<i>P</i> , <i>T</i> :	Case 1		Case 2		Case 3		
	1.5 GPa, 1250°C		2.5 GPa, 1400°C		1 GPa, 1290°C		
Source rock:	M5-40	M7-16	M5-40	M7-16	M5-40	M7-16‡	Bri2§
Run no.:*	P40-15 (97)	P16-15 (126)	P40-25 (115)	P16-25 (98)	P40-10 (76)	P16-10 (83)	
Assemblage:†	cpx, opx, sp, liq	cpx, ol, sp, liq	cpx, gt, liq	cpx, gt, liq	cpx, ol, liq	liq	cpx, opx, ol, liq
<i>F</i> :†	13.5 (12)	9.4 (9)	4.5 (6)	21.8 (21)	84.6 (36)	100	10.5
SiO ₂	50.6 (5)	41.6 (5)	48.7 (6)	39.1 (5)	49.8 (4)	43.6	49.2
TiO ₂	1.08 (4)	1.59 (16)	1.90 (17)	2.36 (18)	0.61 (12)	0.75	0.50
Al ₂ O ₃	19.7 (4)	14.6 (3)	14.6 (3)	10.4 (3)	14.9 (3)	13.7	16.83
Cr ₂ O ₃	0.00 (4)	0.01 (8)	0.01 (8)	0.01 (8)	0.11 (4)	0.07	—
FeO	10.0 (4)	21.8 (5)	12.2 (4)	22.2 (5)	8.3 (3)	14.5	6.5
MnO	0.15 (14)	0.36 (12)	0.19 (8)	0.37 (14)	0.19 (8)	0.30	0.01
MgO	5.6 (2)	7.5 (2)	8.4 (2)	10.6 (4)	11.6 (3)	12.5	13.1
CaO	6.7 (4)	9.8 (4)	8.4 (3)	12.8 (4)	12.5 (4)	13.8	12.1
Na ₂ O	5.40 (2)	2.46 (19)	4.15 (25)	1.94 (16)	1.98 (14)	0.75	1.71
K ₂ O	0.53 (10)	0.32 (10)	1.42 (16)	0.18 (8)	0.08 (4)	0.03	—
Total	98.0 (8)	99.0 (13)	98.7 (6)	97.8 (8)	99.0 (5)	—	—
Mg-no.	50.7 (11)	38.0 (6)	54.9 (10)	46.0 (14)	71.3 (12)	60.6	78.2
Ne/Ol/Hy/	5.7/21.4/0/	8.3/35.8/0/	8.3/22.3/0/	8.9/39.9/0/	0/16.2/9.2/	2.3/31.7/0/	0/15.2/13.1/
Di/Fds¶	4.7/66.2	17.6/35.4	20.5/45.3	20.7/19.1	24.6/48.8	28.2/36.3	17.3/52.7

All compositions are normalized to a sum of 100% (the average total of electron probe analyses before normalization is reported in the column 'Total'). For a given dataset, we calculated both the statistical dispersion (as measured by 2σ , where σ is the standard deviation) and the analytical error (following Ancy *et al.*, 1978), and we selected the largest of these two values as an estimation of the error. The errors (in parentheses) are given in terms of the least unit cited; for example, 50.6 (5) and 1.90 (17) represent 50.6 ± 0.5 and 1.90 ± 0.17 , respectively.

*The first term in the run number corresponds to the bulk composition (P40 for pyroxenite M5-40; P16 for pyroxenite M7-16), the second term to the pressure (in kbar); the run duration (in hours) is given in parentheses after the run number. Experiments P40-10, P40-15, P16-10 and P16-15 are from Lambart *et al.* (2009a) and correspond to their runs 40-A1, 40-E2, 16-A1, and 16-A2, respectively.

†Equilibrium phase assemblage and degree of melting *F* (wt %) in the run products.

‡Superliquidus experiment: the composition listed is the bulk-rock composition (from Table 1).

§Theoretical equilibrium phase assemblage, melting degree, and melt composition of peridotite Bri2 at 1290°C, 1 GPa, and f_{O_2} of FMQ - 1 as predicted by pMELTS (as pMELTS significantly underestimates the degree of melting of peridotites, the calculation was performed at 1350°C; see text for further explanation).

¶CIPW norms.

model underestimates the grossular component in Gt (Smith & Asimow, 2005), but it predicts equilibrium of pyroxenite-derived melt with the same assemblage as in the experiments. Conversely, the new model yields a Gt-bearing paragenesis down to pressures as low as 1.5 GPa.

- (4) We considered that the pyroxenite-derived melt reacts with surrounding peridotite at the *P–T* conditions of its formation. However, the degree of melting of the peridotite is underestimated by pMELTS calculations compared with experimental data (Ghiorso *et al.*, 2002). To circumvent this difficulty, our calculations

were performed 60°C above the experimental temperature: for example, for melts experimentally produced at 1.5 GPa and 1250°C (case 1), the impregnation reaction was calculated with pMELTS at 1.5 GPa and 1310°C.

- (5) We did not include Cr₂O₃ in the bulk compositions used for the calculations. Incorporation of Cr₂O₃ in solid phases is oversimplified by pMELTS (e.g. it is neglected in pyroxene and garnet; see Asimow *et al.*, 1995); as a result, the stability range of spinel is strongly overestimated when Cr₂O₃ is included in the bulk composition.

- (6) We chose to consider MnO as a major element (rather than a trace) because this choice yields thermodynamic results more consistent with experimental ones.
- (7) Potassium was considered as a trace element because, as a major element, it is handled incorrectly in the subsolidus assemblage when feldspar is absent (Asimow & Ghiorso, 1998).

Experimental approach

Experimental rationale

Two series of experiments were performed in a piston-cylinder apparatus. The first investigated the partial melting of pyroxenites M5-40 and M7-16 to determine their melt compositions at 2.5 GPa and 1400°C (experiments P40-25 and P16-25, respectively, in Table 2). The second series was aimed at validating pMELTS calculations using an independent approach. This validation was required because pMELTS is calibrated only for peridotite compositions (Ghiorso *et al.*, 2002). *P–T* conditions and starting compositions were chosen to reproduce and complete our calculations of peridotite–pyroxenite interactions in a subsolidus lithospheric mantle (case 1). Four experiments were performed:

- (1) Experiment Bri2-15 was run to determine the initial mode (before impregnation) of peridotite Bri2 at 1.5 GPa and 1250°C.
- (2) Impregnation experiments I40-15, I16-15 and I16-10 were carried out to characterize the equilibrium phase assemblage after impregnation of peridotite Bri2 with an equal mass of liquid from pyroxenite M5-40 (I40-15) or M7-16 (I16-15 and I16-10). I40-15 and I16-15 were run at 1.5 GPa and 1250°C. I16-10 was run at the same temperature but at a lower pressure (1 GPa) to cross the solidus of the peridotite mantle and to estimate the role of the physical state of the mantle (subsolidus vs partially melted) on reactions.

Starting materials

Fine powders of natural pyroxenites M5-40 and M7-16, and peridotite Bri2 (Table 1) were used as starting materials in experiments P40-25, P16-25, and Bri2-15, respectively. The starting materials for the impregnation experiments were homogeneous mixtures in equal proportions of peridotite Bri2 and either gel 40 or gel 16 (Table 3). Synthetic gels 40 and 16 are close to the equilibrium partial melts of pyroxenites M5-40 and M7-16, respectively, at 1.5 GPa and 1250°C, as determined by Lambart *et al.* (2009a; experiments P40-15 and P16-15 in Table 2). As it is very difficult to prepare a gel composition exactly matching a given chemical composition, there are

Table 3: Gels (40, 16) and peridotite–gel mixtures (I40, I16) used as starting materials in the impregnation experiments (all compositions are normalized to 100 wt %)

	Gel 40	I40	Gel 16	I16
SiO ₂	52.17	48.66	39.82	42.48
TiO ₂	1.12	0.59	1.70	0.89
Al ₂ O ₃	18.41	11.71	11.8	7.23
Cr ₂ O ₃	0.00	0.14	0.03	0.15
FeO	11.07	9.21	24.64	16.12
MnO	0.16	0.14	0.28	0.201
MgO	5.32	23.18	8.49	25.11
CaO	5.93	3.51	12.06	7.14
Na ₂ O	5.24	2.62	1.01	0.60
K ₂ O	0.57	0.28	0.18	0.09
Mg-no.	46.1		38.1	
Ne/Ol/Hy/	1.1/22.4/0/		4.6/39.0/0/	
Di/Fds*	3.7/70.6		23.7/27.1	

Gel 40 reproduces the principal features (alkali-rich and Ne-normative basalt) of the glass composition analysed in the partial melting experiment of pyroxenite M5-40 at 1.5 GPa and 1250°C (P40-15; Table 2); gel 16 reproduces the principal features (basanitic composition) of the glass composition analysed in the partial melting experiment of pyroxenite M7-16 at 1.5 GPa and 1250°C (P16-15; Table 2). Gel compositions were analysed by ICP-AES at Laboratoire Magmas et Volcans. Starting mixtures I40 and I16 were prepared by mixing in equal proportions powdered peridotite Bri2 (Table 1) and either gel 40 or gel 16, respectively. *CIPW norms.

some differences between gels 40 and 16 and the glass analysed in experiments P40-15 and P16-15, respectively. Gels and experimental glasses share, however, the same principal features: a composition of alkali-rich and Ne-normative basalt for gel 40 and P40-15 glass; a basanitic composition for gel 16 and P16-15 glass.

The two pyroxenites and the peridotite were crushed in an agate mortar, and then ground under ethanol in an agate micronizing mill to reduce the grain size to 2–4 µm. The two gels were prepared using the method of Luth & Ingamells (1965). Tetra-ethyl orthosilicate (TEOS) was used as a source for SiO₂ and titrated nitrate aqueous solutions for the other oxides. These solutions were obtained by dissolution in 10 M HNO₃ of either metals (Al, Fe, Mn, Mg) or carbonates (Ca, Na, K) or ammonium salts (Ti, Cr). Rock powders and synthetic gels were all fired for 6 h at 900°C in a CO₂–H₂ atmosphere with an oxygen fugacity between the magnetite–wüstite and iron–wüstite buffers ($f_{\text{O}_2} = 10^{-15.91}$ bar). The starting materials were stored under vacuum to reduce water adsorption.

Experimental and analytical techniques

Experiments were carried out either in a non-end-loaded, $\frac{3}{4}$ inch piston-cylinder apparatus ($P=1\text{--}1.5$ GPa), or in an end-loaded, $\frac{1}{2}$ inch piston-cylinder apparatus ($P=2.5$ GPa). From outside to inside, $\frac{3}{4}$ inch assemblies consist of a NaCl cell wrapped in a lead foil, an outer Pyrex cylinder, a graphite furnace, and an inner Pyrex cylinder. To minimize the amount of adsorbed water, all the pieces of the piston-cylinder assemblies were fired at high temperature, and then stored at 150°C . We used double sample capsules made of graphite (inside) and platinum (outside). Capsules are placed inside the inner Pyrex cylinder, between a rod and a sheath of crushable MgO, and lie at the hot spot of the assembly. Temperature is controlled by a calibrated $\text{W}_{95}\text{Re}_5\text{--}\text{W}_{74}\text{Re}_{26}$ thermocouple. The thermocouple tip is stuck into the MgO sheath and is separated from the sample capsule by a 0.5 mm thick hard alumina disc [see Laporte *et al.* (2004) and Lambart *et al.* (2009b) for technical details]. The $\frac{1}{2}$ inch assemblies are similar except that: (1) they do not include an inner Pyrex cylinder; (2) the thermocouple tip is separated from the platinum capsule by a 0.6 mm thick crushable MgO disc; (3) the capsule is placed into a thin-walled MgO sheath to avoid direct contact between the outer platinum container and the furnace.

The ‘microdike’ technique (Laporte *et al.*, 2004) was used to analyse the composition of liquids in equilibrium with mineral phases: this technique relies on the extraction of small volumes of liquid from the partially molten sample into fractures that formed inside the inner graphite container at the beginning of the experiments. A few microdikes were observed in all experiments (Fig. 1), both at the top and at the bottom of the sample chamber. As the thermal gradient in our assemblies is small ($\sim 5^\circ\text{C}$ across the sample chamber), liquid compositions are homogeneous throughout the sample chamber and there are no significant differences between glass analysed in upper and lower microdikes (Lambart *et al.*, 2009b, and unpublished data). Microdike sizes vary from tens to hundreds of micrometres in length and from a few micrometres to hundreds of micrometres in width. These lengths are smaller than the thickness of the graphite walls ($0.8\text{--}0.9$ mm in $\frac{3}{4}$ inch assemblies and $1.1\text{--}1.2$ mm in $\frac{1}{2}$ inch assemblies) making the contact between melt and platinum container very unlikely. A major advantage of the microdike technique is that it works down to very low degrees of melting ($\leq 1\%$; Laporte *et al.*, 2004) as the volume of melt extracted into the microdikes is small compared with total sample volume.

At the end of an experiment, the capsule was enclosed in epoxy, sectioned lengthwise, polished and carbon-coated. Textures and phase assemblages were characterized using a JEOL JSM-5910 LV scanning electron microscope. Phase compositions were analysed with a Cameca SX100

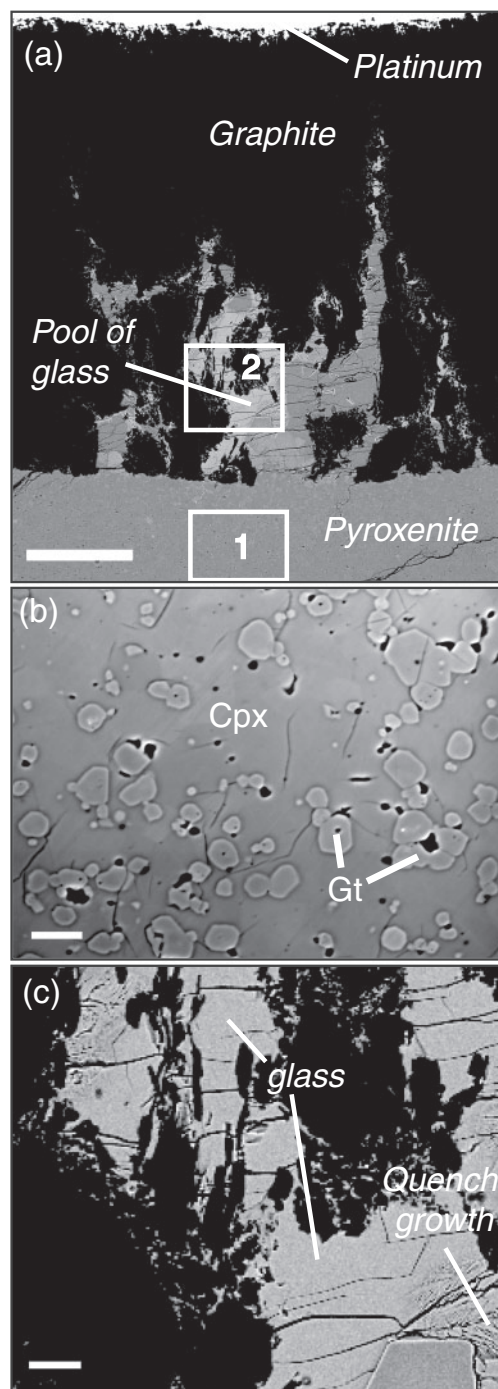


Fig. 1. (a) Backscattered electron image showing microdikes in a high-pressure experiment carried out in a $\frac{1}{2}$ inch piston-cylinder apparatus (run P40-25; 2.5 GPa and 1400°C): the graphite container is black and the partially molten pyroxenite grey; the basaltic microdikes contain large pools of glass and large crystals. (b) Close-up view of white square no. 1 in (a): the phase assemblage of the partially molten pyroxenite is $\text{Cpx} + \text{Gt} + \text{Liq}$; the interstitial melt is not perceptible owing to the relatively low melt fraction ($4\text{--}5\%$) and to the growth of quench Cpx at the end of the experiment. (c) Close-up view of the white square no. 2 in (a) showing a large pool of glass not affected by the growth of quench crystals. Scale bars: $200\ \mu\text{m}$ in (a); $10\ \mu\text{m}$ in (b) and (c).

electron microprobe. A 15 kV accelerating voltage, a 15 nA beam current, counting times of 20 s for Ni, Cr and Ti, and of 10 s for other elements, and a focused beam were used for crystalline phases. For glass analyses, the beam current was lowered to 8 nA and a beam size of 5 μm was used to minimize sodium loss. In most cases, the analytical totals were good (98–100 wt %), typical of basaltic glasses in nominally anhydrous piston-cylinder experiments. The relatively low analytical total of glass in the Il6-15 run (97.3 wt %) could be explained by a more significant amount of dissolved volatiles owing to (1) the low amount of melt (6.6%), and (2) the use of gel in the starting material, a highly hygroscopic material that, despite the great care taken, is almost impossible to maintain in a fully dry state. The proportions of liquid and solid phases best fitting the bulk composition of the starting material were calculated using a mass-balance program modified from Albarède & Provost (1977). Table 4 summarizes the experimental conditions and the phase proportions and compositions in the run products.

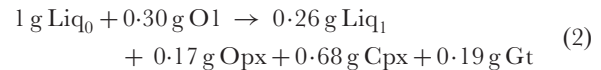
THERMODYNAMIC RESULTS

Computing the impregnation reactions

Impregnation calculations consist in adding from 5 to 100 g of pyroxenite-derived liquid to 100 g of peridotite, in steps of 5 g. After each impregnation step, we compared the equilibrium phase assemblage predicted by pMELTS with the initial phase assemblage of peridotite Bri2. Equilibrium phase assemblages at the end of the impregnation process (100 g of liquid added to 100 g of peridotite, i.e. a melt–rock ratio of unity) are given in Table 5 for the two pyroxenite-derived liquids and the three P – T sets considered in this study; the initial phase assemblages are shown for comparison. To illustrate the evolution of the phase assemblage during impregnation, we plotted the mass variation, Δm , of each phase as a function of the mass m_{Liq_0} of added liquid (Fig. 2); Δm is the difference between the mass of a phase in the impregnated peridotite and its initial mass in peridotite Bri2.

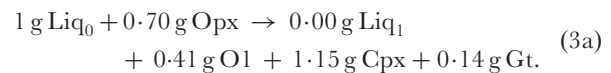
The impregnation reactions were retrieved from the plots in Fig. 2 using a method similar to that used by Baker & Stolper (1994) to compute melting reactions in a fertile peridotite with increasing temperature. Retrieval is easy in the case of impregnation by the liquid from pyroxenite M5-40 (Fig. 2a, c, e) because the phase assemblage remains the same from 0 to 100 g of added liquid and each Δm evolves almost linearly with m_{Liq_0} . In this case, the impregnation process may be described by a single reaction whose coefficients are the slopes of the best-fit lines in Fig. 2: a negative slope indicates that the phase is consumed and a positive slope that it is produced. Let us consider, for instance, the impregnation of peridotite Bri2 by the melt from M5-40 at 2.5 GPa and 1400°C, in which case there is massive production of Cpx, to a lesser extent of

Gt and Opx, and Ol dissolution (Fig. 2c). Writing the reactions in grams for 1 g of added liquid, the impregnation process may quantitatively be described by the following reaction:

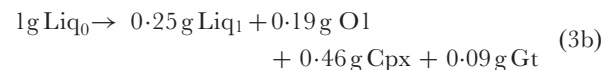


where Liq_0 is the initial melt (from pyroxenite) and Liq_1 is the residual melt after equilibration with peridotite; reaction (2) is valid from 0 to 100 g of added liquid.

The case of the addition of the liquid from pyroxenite M7-16 is not so simple because the plots of Δm vs m_{Liq_0} show slope breaks and steps (Fig. 2b, d and f) that indicate a change of the impregnation reaction in relation to a change of the phase assemblage (exhaustion of a solid phase and/or precipitation of a new phase). At 2.5 GPa and 1400°C (Fig. 2d), for instance, a first reaction operates from 0 to 25 g of added melt and is characterized by the dissolution of a large quantity of Opx and the precipitation of Cpx, Ol, and Gt:



Reaction (3a) results in the exhaustion of Opx at a value of m_{Liq_0} between 25 and 30 g. Then the added liquid interacts with the Opx-free residue according to the reaction



which is valid from 30 to 100 g of added liquid.

It should be noted that the production of a phase during the impregnation process is not systematically linked with an increase of its mass fraction in the final assemblage. Indeed, the mass fraction of a given phase (A) increases only if the mass of phase A produced during impregnation divided by the mass of added liquid exceeds the initial mass fraction of A in the peridotite, a_0 . If c_A (in gram per gram of added liquid) is the coefficient of phase A in the impregnation reaction, then the mass fraction of A increases only if $c_A > a_0$. For instance, let us consider the case of reaction (3a), which produces 0.41 g of Ol, 1.15 g of Cpx, and 0.14 g of Gt per gram of added liquid. The initial mass fractions of Ol, Gt, Opx, and Cpx in Bri2 at 2.5 GPa and 1400°C are equal to 0.652, 0.034, 0.206, and 0.108, respectively (Table 5), so c_A is larger than a_0 for Cpx and Gt, but smaller than a_0 for Ol. Using reaction (3a), we can compute the masses after impregnation of 100 g of peridotite by 25 g of liquid: 75.45 g of Ol, 6.9 g of Gt, 3.1 g of Opx, and 39.55 g of Cpx; that is, in terms of mass fractions, 0.604, 0.055, 0.025, and 0.316 for Ol, Gt, Opx, and Cpx, respectively. As expected, the mass fractions of Cpx and Gt increased during impregnation, but that of Ol decreased slightly. This is the explanation for the slight

Table 4: Summary of run information: pressure, temperature, duration, phase proportions and compositions (wt %)

<i>n</i>	Mode	SiO ₂	TiO ₂	Al ₂ O ₃	Cr ₂ O ₃	FeO	MnO	MgO	CaO	Na ₂ O	K ₂ O	Total	Mg-no.	(Fe-Mg) K _D *
<i>Run P40-25 (2.5 GPa, 1400°C), 115h</i>														
liq (10)	4.5 (6)	48.69 (56)	1.90 (17)	14.61 (29)	0.01 (8)	12.22 (39)	0.19 (8)	8.36 (24)	8.44 (32)	4.15 (25)	1.42 (16)	98.7 (6)	54.9 (10)	
cpx (8)	71.8 (23)	51.44 (42)	0.45 (6)	8.83 (70)	0.14 (7)	7.74 (38)	0.19 (6)	16.03 (87)	13.38 (58)	1.79 (16)	0.00 (0)	99.3 (6)	78.7 (10)	0.33
gt (6)	23.7 (22)	41.24 (95)	0.38 (13)	23.1 (11)	0.17 (18)	11.58 (30)	0.32 (5)	17.22 (74)	5.90 (76)	0.09 (21)	0.01 (3)	100.5 (5)	72.6 (13)	0.46
<i>Run P16-25 (2.5 GPa, 1400°C), 98h</i>														
liq (12)	21.8 (21)	39.09 (48)	2.36 (18)	10.39 (25)	0.01 (8)	22.23 (49)	0.37 (14)	10.63 (43)	12.78 (39)	1.94 (16)	0.18 (8)	98.1 (8)	46.0 (14)	
cpx (8)	46.2 (20)	48.66 (60)	0.54 (6)	9.80 (78)	0.09 (3)	8.31 (34)	0.16 (6)	12.74 (43)	18.80 (38)	0.90 (9)	0.00 (1)	100.2 (8)	73.2 (11)	0.31
gt (5)	32.0 (17)	40.26 (39)	0.38 (31)	22.80 (25)	0.07 (3)	14.8 (17)	0.45 (5)	13.10 (94)	8.1 (17)	0.01 (2)	0.01 (3)	100.9 (7)	61.3 (18)	0.54
<i>Run Bri2-15 (1.5 GPa, 1250°C), 137h</i>														
ol (6)	65.0 (35)	41.08 (40)	0.01 (2)	0.08 (4)	0.10 (6)	9.30 (26)	0.13 (6)	49.1 (44)	0.21 (5)	—	—	100 (1)	90.4 (3)	
opx (7)	21.7 (48)	54.23 (66)	0.12 (6)	5.86 (90)	0.78 (11)	5.70 (20)	0.12 (6)	31.25 (60)	1.85 (41)	—	—	100.0 (5)	90.7 (2)	
cpx (8)	13.1 (25)	51.91 (63)	0.33 (8)	6.78 (51)	1.12 (20)	3.55 (50)	0.11 (10)	18.1 (13)	17.0 (20)	1.09 (12)	0.01 (1)	100.3 (6)	90.1 (9)	
sp (3)	0.2 (6)	0.32 (7)	0.18 (9)	55.1 (28)	13.8 (32)	8.72 (38)	0.11 (7)	21.70 (79)	0.03 (5)	0.01 (3)	—	98.0 (8)	81.6 (12)	
<i>Run I40-15 (1.5 GPa, 1250°C), 116h</i>														
liq (9)	31.8 (19)	51.41 (58)	1.13 (14)	19.43 (41)	0.05 (9)	6.96 (31)	0.09 (8)	6.74 (40)	5.84 (30)	7.44 (43)	0.91 (13)	98.1 (18)	63.3 (17)	
ol (5)	16.1 (20)	40.31 (39)	0.05 (6)	0.10 (4)	0.11 (9)	12.98 (30)	0.14 (6)	46.10 (24)	0.20 (7)	—	—	100.5 (5)	86.3 (3)	0.27
opx (6)	42.7 (33)	52.70 (78)	0.35 (12)	7.4 (12)	0.19 (8)	9.38 (26)	0.16 (7)	27.80 (72)	1.99 (34)	—	—	100.1 (7)	84.1 (5)	0.33
cpx (6)	6.7 (15)	51.45 (42)	0.68 (8)	9.28 (22)	0.28 (7)	6.86 (21)	0.16 (6)	18.17 (26)	11.55 (40)	1.54 (11)	0.01 (2)	100.3 (7)	82.5 (3)	0.37
sp (2)	2.8 (7)	0.22 (5)	0.35 (12)	59.4 (37)	8.5 (41)	11.19 (85)	0.14 (7)	20.1 (16)	0.05 (5)	0.00 (0)	—	98.7 (9)	76.2 (28)	0.54
<i>Run I16-15 (1.5 GPa, 1250°C), 97h</i>														
liq (10)	6.6 (6)	44.42 (55)	3.99 (20)	15.29 (30)	0.02 (8)	15.23 (42)	0.16 (8)	7.82 (28)	8.52 (32)	3.33 (20)	1.22 (16)	97.3 (11)	47.8 (12)	
ol (7)	43.2 (14)	38.47 (39)	0.07 (6)	0.09 (4)	0.03 (9)	23.04 (30)	0.25 (6)	37.72 (24)	0.35 (7)	—	—	99.8 (13)	74.5 (1)	0.31
opx (6)	0.1 (30)	51.7 (15)	0.51 (20)	6.6 (15)	0.21 (8)	13.27 (88)	0.20 (7)	25.5 (13)	2.02 (40)	—	—	100.0 (9)	77.4 (29)	0.27
cpx (10)	46.6 (24)	49.28 (68)	1.21 (17)	8.77 (81)	0.22 (5)	9.80 (40)	0.20 (6)	16.19 (86)	13.5 (13)	0.86 (8)	0.01 (2)	100 (1)	74.6 (7)	0.31
sp (4)	3.6 (4)	0.31 (12)	0.85 (17)	58.0 (43)	4.7 (42)	19.35 (88)	0.12 (6)	16.46 (72)	0.11 (7)	0.01 (3)	—	98.5 (9)	60.3 (20)	0.60
<i>Run I16-10 (1 GPa, 1250°C), 84h</i>														
liq (6)	41.4 (7)	46.26 (71)	1.99 (17)	15.05 (77)	0.10 (9)	14.47 (57)	0.19 (9)	8.78 (11)	11.33 (37)	1.56 (14)	0.25 (8)	99.9 (18)	55.5 (40)	
ol (14)	49 (6)	38.95 (39)	0.03 (4)	0.08 (4)	0.10 (6)	20.27 (32)	0.22 (8)	39.99 (31)	0.36 (6)	—	—	100.3 (6)	77.9 (4)	0.31
cpx (14)	9.5 (13)	49.84 (68)	0.65 (15)	7.35 (91)	0.73 (15)	8.47 (56)	0.17 (8)	17.14 (65)	15.33 (95)	0.32 (7)	0.00 (2)	100.3 (9)	73.3 (10)	0.30
sp (6)	0.1 (2)	0.19 (9)	0.44 (6)	56.8 (18)	9.2 (18)	16.36 (25)	0.13 (10)	16.78 (27)	0.13 (9)	0.01 (3)	—	99.8 (4)	64.7 (3)	0.59

For all experiments, the run number is built as follows: the first term is the bulk composition and the second term is the pressure (in kbar). In this way, runs P40-25 and P16-25 are partial melting experiments on pyroxenites M5-40 and M7-16, respectively. Run Bri2-15 is a subsolidus experiment to determine the mode of peridotite Bri2 at 1.5 GPa and 1250°C. Impregnation experiments I40-15, I16-15, and I16-10 were performed to characterize the equilibrium phase assemblage after impregnation of peridotite Bri2 by an equal mass of liquid from pyroxenite M5-40 (I40-15) or M7-16 (I16-15, I16-10). Phase compositions were analysed with the electron microprobe; *n* is the number of analyses. All compositions are normalized to a sum of 100 wt % (the analytical total before normalization is reported in the column 'Total'). For a given phase in a given sample, we calculated the statistical dispersion of the dataset (as measured by 2σ , where σ is the standard deviation) and the analytical error (following Ancy *et al.*, 1978), and we selected the largest of these two values as an estimation of the error. The errors (in parentheses) are given in terms of the least unit cited. Modes (in wt %) are calculated using a mass-balance program modified from Albarède & Provost (1977). The number in parentheses is 2σ , given in terms of the least unit cited.

*Fe-Mg exchange coefficients between mineral and melt: $[K_D = (\text{Fe}/\text{Mg})^{\text{mineral}} / (\text{Fe}/\text{Mg})^{\text{melt}}]$.

Table 5: *pMELTS* results: masses of solid phases and liquid in the peridotite before impregnation (columns 'Bri2') and after impregnation by an equivalent mass of melt from pyroxenite M5-40 (columns 'Bri2 + M5-40') or M7-16 (columns 'Bri2 + M7-16')

<i>P</i> , <i>T</i> (<i>T</i> _{pMELTS}):*	Case 1			Case 2			Case 3		
	1.5 GPa, 1250°C (1310°C)			2.5 GPa, 1400°C (1460°C)			1 GPa, 1290°C (1350°C)		
	Bri2	Bri2 + M5-40	Bri2 + M7-16	Bri2	Bri2 + M5-40	Bri2 + M7-16	Bri2	Bri2 + M5-40	Bri2 + M7-16
Ol	63.0	25.6	65.6	65.2	33.7	89.2	66.4	64.3	80.7
Gt	0	0	0	3.4	21.6	10.6	0	0	0
Opx	25.0	71.6	0	20.6	35.8	0	21.8	18.8	0
Cpx	10.3	35.4	100.2	10.8	80.5	80.4	1.3	12.8	18.8
Sp	1.7	8.0	6.6	0	0	0	0	0	0
Liq	0	55.4	26.0	0	28.4	18.4	10.5	104.1	100.5
Reaction†		4	5a and 5b		2	3a and 3b		6	7a and 7b

For Bri2, masses are given for 100 g of rock; for mixtures Bri2 + M5-40 and Bri2 + M7-16, masses are given for 200 g of rock.

**P*–*T* conditions of the three cases considered. Temperature in parentheses is the temperature at which the calculations were performed: as *pMELTS* significantly underestimates the degree of melting of peridotites in comparison with experimental data (Ghiorso *et al.*, 2002), the calculations were made 60°C above the nominal temperature.

†This line gives the number of the impregnation reaction in the text.

decrease of the Ol percentage between 0 and 25 g of added liquid in the Ol–Opx–Cpx triangle (Fig. 3b).

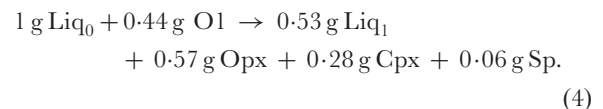
Finally, we note that in some cases, the choice of a linear approximation may be questioned. In Fig. 2b, Cpx and Opx show a variation of their reaction coefficients (i.e. slope variation) not correlated to a change of assemblage. This highlights a limitation for the method of calculation. This particular case will be discussed subsequently.

Case 1 (1.5 GPa and 1250°C)

Case 1 corresponds to a situation where bodies of partially molten pyroxenite are surrounded by unmolten peridotite that prevents extraction of the pyroxenite-derived melts at low degrees of melting. At 1.5 GPa and 1250°C, both M5-40 and M7-16 have degrees of melting close to 10% (Table 2). We stress, however, that the main conclusions below do not depend on the exact degree of melting of the pyroxenite (and so on temperature) as long as it lies between 0% and 15–20%: within this range, the partial melts from pyroxenites M5-40 and M7-16 are Ne-normative and keep the same compositional characteristics, namely silica- and alkali-rich for M5-40 and silica-poor for M7-16 (see table 1 in Lambart *et al.*, 2009a). In terms of temperature, *T* must be lower than ~1270°C (at 1.5 GPa) to satisfy the constraint that the surrounding peridotite is subsolidus.

Impregnation of peridotite Bri2 by pyroxenite-derived melts at 1.5 GPa and 1250°C leads to major modifications of the modal composition of the solid assemblage. In the

case of M5-40 melt (Fig. 2a), the impregnation leads to Ol dissolution and production of Opx, Cpx, and a little spinel (Sp). The reaction remains unchanged from 0 to 100 g of added liquid:



It should be noted that almost half the added melt is consumed in this reaction. The modal compositions of the impregnated rocks are projected onto the Ol–Opx–Cpx triangle in Fig. 3a. The evolution is dominated by the drop of the Ol component, which leads to a transition of the solid assemblage from the lherzolite field to the Ol websterite field; this transition occurs at a melt–rock ratio of 0.40 (i.e. $m_{\text{Liq}_0} = 40 \text{ g}$).

In the case of the impregnation by the melt from M7-16, the evolution is markedly different (Fig. 2b). From 0 to 45 g of added melt, Opx is dissolved, a large quantity of Cpx and small quantities of Ol and Sp are produced, and most of the added liquid is consumed. After the disappearance of Opx (between 45 and 50 g of added melt), Ol switches from the product side to the reactant side of the reaction. However, before the Opx exhaustion, the evolution lines of Opx and Cpx mass variations are curved (Fig. 2b). To explain this nonlinear evolution, Fig. 4a illustrates the mass variation of bulk pyroxene (Cpx + Opx) as a function of the mass of added liquid between 0 and

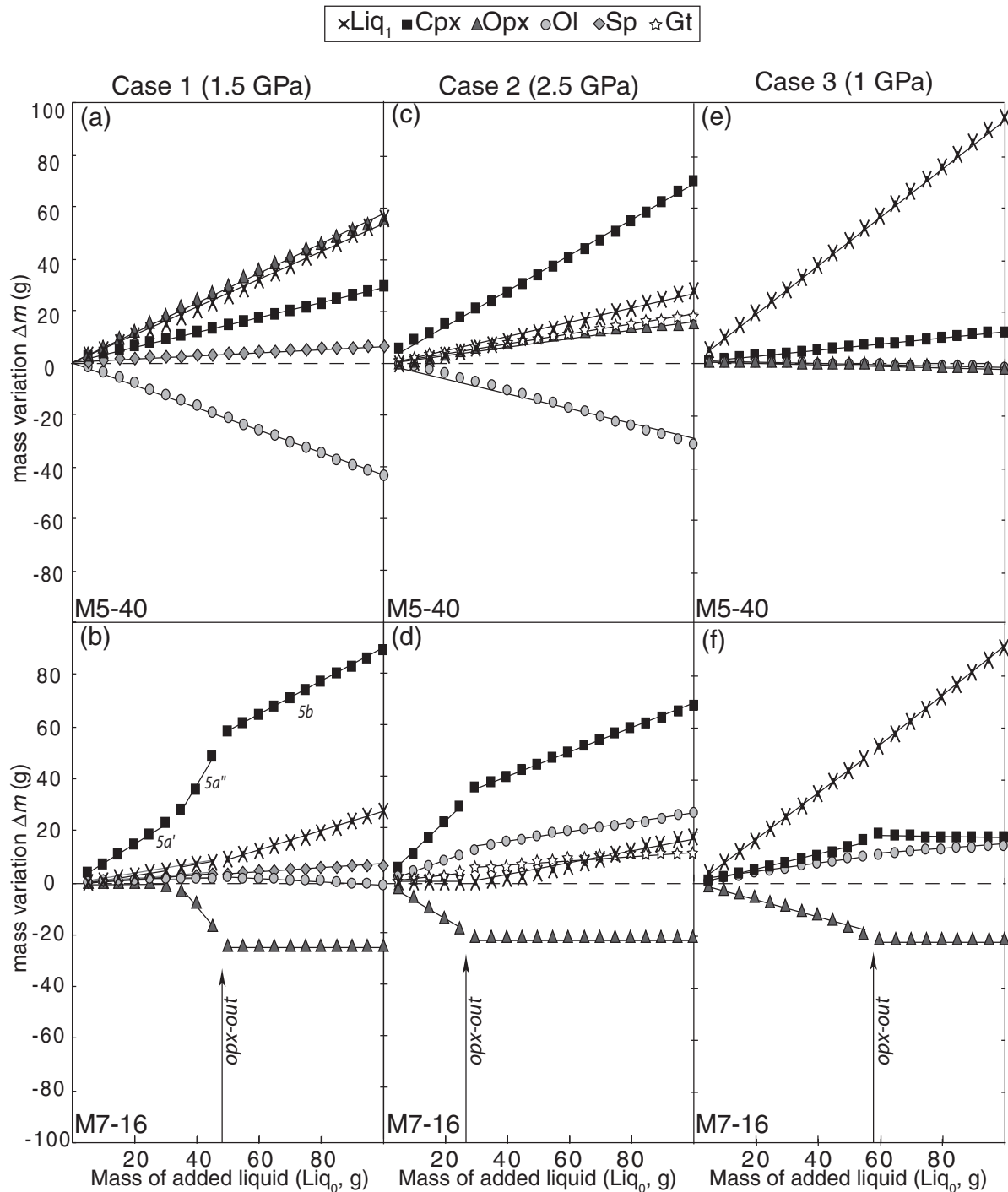


Fig. 2. Thermodynamic results: impregnation of 100 g of peridotite Bri2 by 0–100 g of liquid (Li_0) from pyroxenite M5-40 (upper row) or pyroxenite M7-16 (lower row). (a, b) Case 1: 1.5 GPa and 1310°C; (c, d) case 2: 2.5 GPa and 1460°C; (e, f) case 3: 1 GPa and 1350°C. The calculations were made 60°C above nominal temperatures (i.e. 1250, 1400, and 1290°C for cases 1, 2, and 3, respectively) because pMELTS underestimates the melting degree of peridotite at a given P and T (Ghiorso *et al.*, 2002). The abscissa is the mass m_{Li_0} of liquid Li_0 added to the system. The ordinate is the mass variation, Δm , of the different phases: for a given mass of added liquid, Δm is the difference between the mass of a phase in the impregnated peridotite and its initial mass in peridotite Bri2; line $\Delta m = 0$ is shown by dashes. Symbols are as follows: crosses, residual melt after equilibration (Li_1); squares, Cpx; triangles, Opx; circles, Ol; diamonds, Sp; stars, Gt. Straight lines are best-fit lines used to compute the impregnation reactions: the slope is positive when the phase is produced, negative when it is consumed; a slope break marks a reaction change in relation to the exhaustion of a solid phase and/or the precipitation of a new phase; for M7-16 three sets of best-fit lines are plotted, corresponding to reactions (5a'), (5a'') and (5b) (see text).

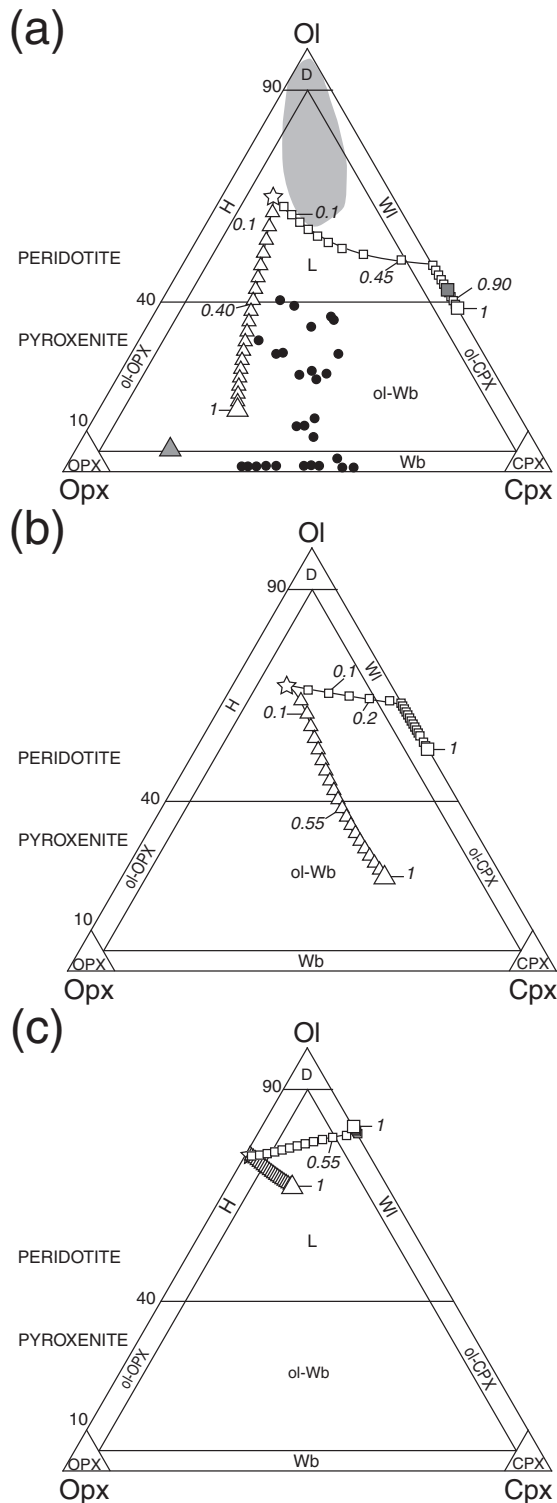
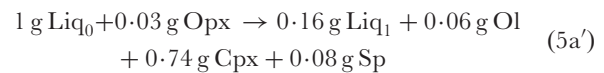


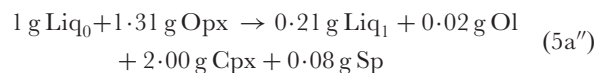
Fig. 3. Projection onto the Ol–Opx–Cpx triangle of the modal compositions of peridotites impregnated by 0–100% of pyroxenite-derived melt at (a) 1.5 GPa and 1250°C (case 1), (b) 2.5 GPa and 1400°C (case 2), and (c) 1 GPa and 1290°C (case 3). Stars, initial peridotite Bri2; triangles, rocks impregnated by melt from pyroxenite M5-40; squares, rocks impregnated by melt from pyroxenite M7-16. Each symbol represents the addition of 5 g of melt to the system (the initial

45 g). The almost perfect linear correlation ($R^2 > 0.99$) shows that the mass changes in Cpx and Opx are strongly interdependent. We also plotted $\text{Ca}/(\text{Ca} + \text{Mg} + \text{Fe})$ in Cpx as a function of Δm for Cpx (Fig. 4b): the correlation between the mass variation of Cpx and its composition is linear. Hence, Fig. 4 emphasizes a limitation of the method: when a solid phase undergoes important compositional changes, its mass variation is no longer proportional to the amount of added melt. It should be noted, however, that, except in the case discussed above, all regression coefficients of Cpx calculated for a given phase assemblage are higher than 0.9. Accordingly, the linear approximation is appropriate for the calculation of impregnation reactions in most cases.

In the case of Fig. 2b, we subdivided the curve into parts with $R^2 > 0.9$ and we estimated that the reaction evolves from

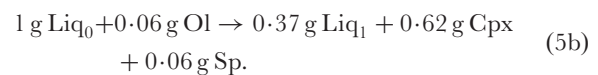


between 0 and 30 g of added melt, to



from 35 g of added melt up to Opx exhaustion.

After the disappearance of Opx (between 45 and 50 g of added melt), mass variations evolve almost linearly according to the reaction



In the Ol–Opx–Cpx triangle (Fig. 3a), reaction between melt from M7-16 and peridotite Bri2 results in a strong increase of the Cpx/Opx ratio, and the solid assemblage moves from the lherzolite field into the wehrlite field (at a melt–rock ratio of ~ 0.45 – 0.50). With reaction (5b), the solid assemblage drifts along the Ol–Cpx side of the triangle toward the Cpx corner, reaching the field of Ol-bearing clinopyroxenites at a melt–rock ratio of ~ 0.90 .

Case 2 (2.5 GPa and 1400°C)

According to pMELTS, the phase assemblage of peridotite Bri2 at 2.5 GPa and 1400°C is a subsolidus Gt lherzolite

(mass of peridotite Bri2 is 100 g). Magma–rock ratios are indicated in italics. In (a), the black circles correspond to group C pyroxenites from Ronda (Remaïdi, 1993; Garrido & Bodinier, 1999; Bodinier *et al.*, 2008), the grey field corresponds to peridotites from Ronda (Remaïdi, 1993; Van der Wal & Bodinier, 1996) and the grey square and triangle correspond to the equilibrium phase assemblages computed for bulk compositions I16 and I40, respectively, at 1.5 GPa and 1310°C (see text for further explanation). D, dunite; H, harzburgite; L, lherzolite; Wl, wehrlite; OPX, orthopyroxenite; CPX, clinopyroxenite; Wb, websterite.

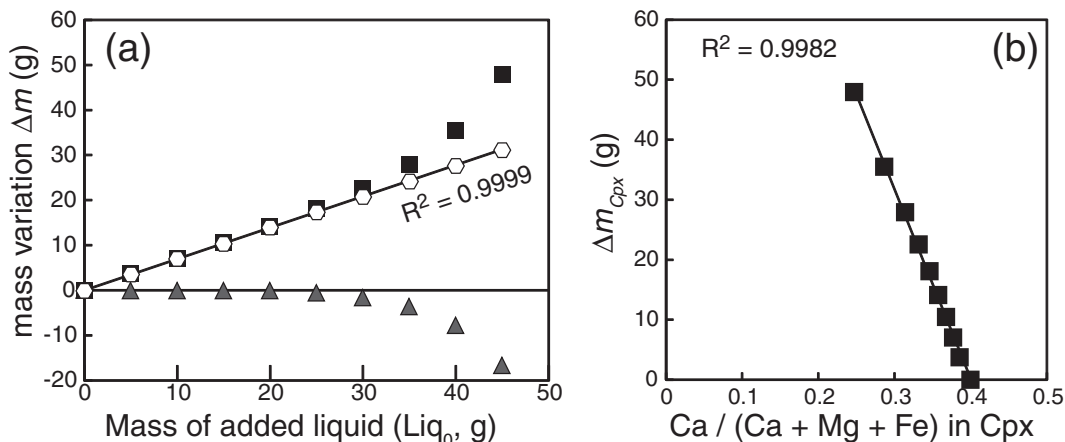


Fig. 4. Impregnation of peridotite Bri2 with the melt from pyroxenite M7-16 in case 1 (1.5 GPa and 1310°C). (a) Mass variation, Δm , of Cpx (squares), Opx (triangles) and Cpx + Opx (hexagons) as a function of the mass of liquid Liq_0 added to the system; the straight line is the best-fit line for the Cpx + Opx correlation. (b) Mass variation of Cpx, Δm_{Cpx} , as a function of molar $\text{Ca}/(\text{Ca} + \text{Mg} + \text{Fe})$ in Cpx; straight line is a best-fit line.

(Table 5). In these P – T conditions, melts from pyroxenites M5-40 and M7-16 are both in equilibrium with Cpx and Gt (runs P40-25 and P16-25, Table 4). As in the previous case, impregnation of peridotite by pyroxenite-derived melts at 2.5 GPa and 1400°C results in a strong modification of the solid phase proportions. In the case of the partial melt from pyroxenite M5-40, impregnation leads to a massive production of Cpx and to a lesser extent of Gt and Opx, and to Ol dissolution (Fig. 2c): for 100 g of added liquid, the impregnation reaction produces 68 g of Cpx, 19 g of Gt, and 17 g of Opx, it consumes 30 g of Ol, and the mass of residual liquid is 26 g [see reaction (2) above]. The evolution of impregnated rocks is marked by a major drop of the Ol component and a significant increase of the Cpx/Opx ratio; the solid assemblage changes from a lherzolite to an Ol websterite at a melt–rock ratio of ~ 0.50 – 0.55 (Fig. 3b). The mass fraction of Gt increases from 3.4% in peridotite Bri2 to 10.8% at a melt–rock ratio of unity (Table 5).

Impregnation of peridotite Bri2 by the melt from pyroxenite M7-16 is also characterized by the crystallization of a large amount of Cpx and a smaller amount of Gt [1.15 and 0.14 g, respectively, per gram of added liquid; reaction (3a)]. As in case 1, however, the behaviours of Ol and Opx are the opposite of those observed with the melt from M5-40: the addition of 1 g of liquid from M7-16 consumes 0.70 g of Opx and precipitates 0.41 g of Ol. Reaction (3a) rapidly leads to the exhaustion of Opx (at a m_{Liq_0} value between 25 and 30 g; Fig. 2d); it is then replaced by reaction (3b), in which the products are Cpx, Ol, and Gt (0.46, 0.19, and 0.09 g, respectively, per gram of added liquid). Residual liquid is absent in reaction (3a) and its mass is small in reaction (3b) (0.25 g). The evolution of impregnated rocks (Fig. 3b) is similar to that

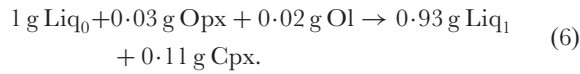
described in case 1, with first an increase of the Cpx/Opx ratio at a nearly constant Ol mode [reaction (3a)], and then a decrease of the Ol mode along the Ol–Cpx side of the Ol–Opx–Cpx triangle [reaction (3b)]; the transition from the lherzolite field to the wehrlite field occurs at a melt–rock ratio slightly larger than 0.2.

Case 3 (1 GPa and 1290°C)

A distinctive feature of case 3 is that peridotite Bri2 is then partially molten: according to pMELTS, at 1 GPa and 1290°C, Bri2 is made of 10.5% liquid in equilibrium with a harzburgitic residue (66.4% Ol, 21.8% Opx, and 1.3% Cpx; Table 5). Another distinctive feature is that the pyroxenites are totally or almost totally molten at these P – T conditions (Table 2). We ran two sets of calculations for case 3. In the first set, we directly added the pyroxenite-derived liquid to the bulk peridotite, as in cases 1 and 2. It may be unrealistic, however, to assume that a large body of partially molten peridotite with a degree of melting of $\sim 10\%$ would not undergo any solid–liquid separation. Indeed, melt migration through peridotites proceeds at degrees of melting from 0.1–1 vol. % (Kohlstedt, 1991; Wark *et al.*, 2003) to 2–3 vol. % (Faul, 1997), depending on the permeability–porosity relationship. To test the effect of melt extraction from the peridotite, we made a second set of calculations, in which most of the melt is removed from the peridotite at each step, just 2% melt being left in the system before the next impregnation step by 5 g of pyroxenite-derived melt. In this way, we simulate the situation where the partial melt from the peridotite is mostly extracted and replaced by the pyroxenite-derived melt (as set 2 yields results very close to those of set 1, only the results of set 1 are shown in Fig. 2e and f).

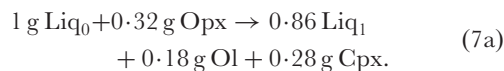
Set 1

Contrary to all previous calculations, the impregnation of peridotite Bri2 by the melt from M5-40 at 1 GPa and 1290°C results in only minor modifications of phase masses. Small quantities of Opx and Ol are dissolved, a small quantity of Cpx is precipitated, and the mass of liquid remains almost unchanged (Fig. 2e):



As the coefficients of Ol and Opx in reaction (6) are small, their proportions in the solid assemblage change little with impregnation: they decrease from 75.1% and 24.5% in Bri2 to 70.1% and 18.2% respectively at a melt–rock ratio of unity. Concurrently, the Cpx proportion increases from 0.3 to 11.7%, and the solid assemblage shifts from the harzburgite to the lherzolite field (Fig. 3c). The minor effect of impregnation predicted by pMELTS in the present case is consistent with the weak compositional contrast between melts from M5-40 and Bri2 at 1 GPa and 1290°C (Table 2): the melt from pyroxenite M5-40 has a composition close to the peridotite-derived melt except for slight differences in CaO and Al₂O₃ contents owing to a higher melting degree of the pyroxenite, and a lower Mg-number.

The melt from M7-16 has a much lower SiO₂ content and a much higher FeO content than the peridotitic melt (Table 2), so we anticipate a more significant effect of impregnation than for M5-40. Indeed, the addition of liquid from M7-16 consumes Opx and precipitates Cpx and Ol (Fig. 2f):



After the disappearance of Opx (between 55 and 60 g of added melt), the effect of impregnation drops dramatically, and the reaction becomes

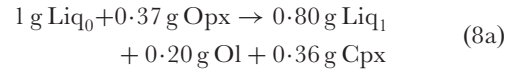


In the Ol–Opx–Cpx triangle (Fig. 3c), the main effect of reaction (7a) is to increase the Ol and Cpx modes at the expense of Opx so that the solid assemblage in the impregnated peridotite goes from the harzburgite field, through the lherzolite field, to the wehrlite field. After the disappearance of Opx, the solid assemblage undergoes only minor changes.

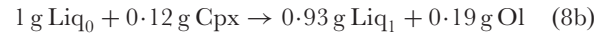
Set 2

In this set of calculations, we extracted partial melt from the bulk composition leaving 2 wt % of melt before launching the next impregnation step. For the melt from M5-40, the reaction with the residual peridotite is exactly

the same as that obtained in the first set [reaction (6)]. For M7-16, the impregnation reactions are



until the disappearance of Opx (between 50 and 55 g of added melt), and then



Despite a slightly higher melt consumption and Ol production in the second set, these two reactions are similar to reactions (7a) and (7b). Hence, the great similarity between the results of sets 1 and 2 suggests that calculations and experiments performed in a closed system where melt stays in equilibrium with the solid assemblage can be applied to the more realistic case where melt is continuously extracted from its source, as expected beneath mid-ocean ridges (e.g. Langmuir *et al.*, 1992).

EXPERIMENTAL RESULTS**Attainment of equilibrium**

Phase assemblages, modes and run durations are given in Table 4. The durations of our experiments (76–137 h) are significantly longer than those in most high-pressure and high-temperature studies (Hirschmann *et al.*, 2008). Although the present set of experiments was not reversed, the following observations indicate that chemical equilibrium was closely approached: (1) despite the presence of unreacted cores ($\leq 5 \mu\text{m}$) in some garnets, most solid phases show no detectable compositional zoning and their compositions are homogeneous throughout the sample chamber; (2) a high degree of microtextural equilibration is observed even at low degrees of melting; (3) Fe–Mg exchange coefficients (Table 4) between solid phases and liquid are consistent with those from the literature; (4) temperatures calculated on the basis of Cpx–liquid equilibrium (Putirka *et al.*, 1996, 2003) are in good agreement with the experimental temperatures (see below). The close approach of chemical equilibrium in our experiments is due to the long run durations, the fine grain size of the starting materials and the highly reactive nature of gel when it is present.

Partial melting experiments of pyroxenites M5-40 and M7-16

The phase assemblage in experiments P40-25 and P16-25 consists of Liq + Cpx + Gt (Fig. 1; Table 4). In run P40-25, the melt fraction is lower (4.5%) than in run P16-25 (21.8%), and the Cpx/Gt ratio is significantly higher (3.0 and 1.4, respectively). Cpx crystals (20–30 μm in size) show no detectable compositional zoning and the compositional variability in a single sample is small. In contrast, Gt sometimes presents unreacted cores and its composition

in a single sample is more variable, probably as a result of incomplete equilibration. Fe–Mg exchange coefficients between Cpx and melt and Gt and melt are 0.32 ± 0.01 and 0.50 ± 0.04 , respectively (Table 4); these coefficients are broadly consistent with those measured in previous pyroxenite partial melting experiments at $P > 2$ GPa (e.g. Kogiso *et al.*, 2003; Kogiso & Hirschmann, 2006). Because Fe and Mg diffusion rates are generally higher than the diffusion rate of other elements (Na, Al, Ca), equilibrium tests based solely on Fe and Mg are not sufficient (e.g. Rhodes *et al.*, 1979; Putirka, 1999). Accordingly, we used Putirka *et al.*'s (1996, 2003) geothermometer, which takes into account most major elements, to test equilibrium between Cpx and melt in our experiments (Fig. 5). There is a good agreement between calculated (T_{calc}) and experimental (T_{exp}) temperatures, as ($T_{\text{calc}} - T_{\text{exp}}$) differences are well within the error of the thermometer ($\pm 45^\circ\text{C}$; Putirka, 2008).

Impregnation experiments: modes, textures, and tests for equilibrium

Composition Bri2 equilibrated at 1.5 GPa and 1250°C is a subsolidus lherzolite with 65% Ol, 22% Opx, 13% Cpx and traces of Sp (run Bri2-15 in Table 4). The phase assemblages in impregnation experiments I40-15 and I16-15 are qualitatively the same: Ol + Cpx + Sp + Opx + Liq, with 31.8% melt in I40-15 and 6.6% in I16-15. The proportions of the solid phases are very different in the two samples, however: the main solid phase in I40-15 is Opx (42.7%), followed by Ol (16.1%), Cpx (6.7%), and Sp (2.8%); the main solid phases in I16-15 are Cpx and Ol (46.6% and 43.2%, respectively), followed by Sp (3.6%) and Opx (trace). The phase assemblage in impregnation experiment I16-10 is Ol + Cpx + Sp + Liq. Compared with I16-15 (same composition and temperature, but a higher pressure of equilibration), sample I16-10 has a larger melt fraction (41.3% vs 6.6%), a slightly larger Ol fraction, and much lower Cpx and Sp fractions (Table 4). In runs Bri2-15 and I16-15 (either subsolidus or with a low melt fraction), grain growth did not play a prominent role, and grains grew only from a few microns in the starting mixture to 2–15 µm in the final product. However, a high degree of textural equilibration was attained owing to the very small grain size of our starting material: microtextures are characterized by polygonal grain shapes with plane or slightly curved grain boundaries, and grain-boundary angles close to 120° as expected in a well-annealed polycrystal (Smith, 1964). In runs I40-15 and I16-10 in which the melt fraction is significantly higher, Ol crystals exceed 20 µm and pyroxene grains can reach a diameter of 10–15 µm.

Fe–Mg exchange coefficients between Ol and melt are equal to 0.30 ± 0.02 , perfectly consistent with values predicted by Toplis' (2005) model (0.31 ± 0.01). Fe–Mg exchange coefficients between Opx and melt and between

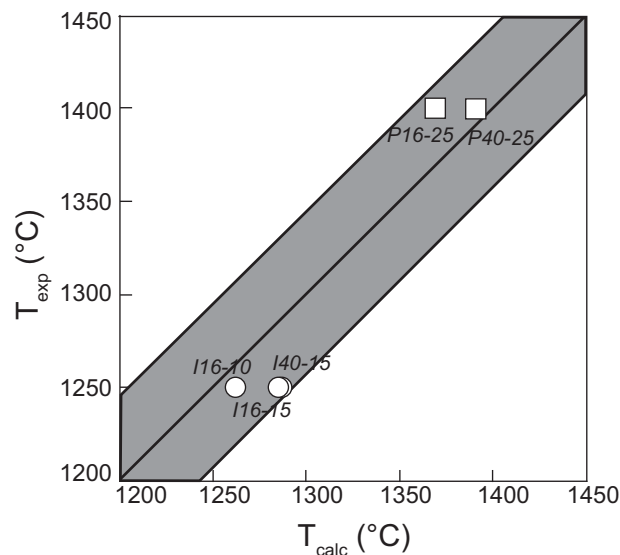


Fig. 5. Comparison between experimental temperatures, T_{exp} and temperatures calculated using the Cpx–liquid geothermometer of Putirka *et al.* (1996, 2003), T_{calc} . Pyroxenite partial melting experiments are represented by squares and impregnation experiments by circles. The grey area indicates the geothermometer uncertainty ($\pm 45^\circ\text{C}$).

Cpx and melt are equal to 0.30 ± 0.04 and 0.33 ± 0.04 , respectively. These values are in agreement with those reported in the peridotite system at the same pressure (Kushiro, 1996; Robinson *et al.*, 1998; Falloon & Danyushevsky, 2000). Finally, the differences between temperatures calculated using Putirka *et al.*'s (1996, 2003) geothermometer and the experimental temperature are within the error bar of the thermometer (Fig. 5), indicating that Cpx–liquid equilibrium is approached in our experiments.

Effect of impregnation on melt composition: experimental insight

The experimental approach allowed us to determine the composition of the residual melt after the impregnation of a subsolidus peridotite by a pyroxenite-derived melt. Melt compositions in runs I40-15, I16-15, and I16-10 are given in Table 4. The main differences between the two initial liquids (high concentrations of SiO_2 , Al_2O_3 and alkalis, and low concentrations of FeO, CaO and MgO in gel 40 compared with gel 16; Table 3) are still visible, though reduced, after equilibration with the peridotite. Thus, the partial melt in run I40-15 is a basaltic trachyandesite according to the total alkali–silica classification (Le Bas *et al.*, 1986) whereas the partial melt in run I16-15 is a basanite and the partial melt in run I16-10 is a low- SiO_2 basalt close to a micro-basalt. In comparison with the initial melt compositions, the liquid phase in all experiments is strongly depleted in FeO and, as MgO shows only little

variation, the impregnation process results in a strong increase of melt-Mg-number: from 46.1 in gel 40 to 63.3 in run I40-15, from 38.1 in gel 16 to 47.8 in run I16-15, and to 55.5 in run I16-10. Other major differences between the initial liquid compositions and the liquid compositions at the end of the impregnation experiments include: (1) an increase of the Na₂O and K₂O concentrations, especially in run I16-15; (2) a strong enrichment in SiO₂ and Al₂O₃, and a depletion in CaO in runs I16-15 and I16-10; (3) a strong increase of TiO₂ in the melt from sample I16-15 (4% vs 1.7% in gel 16). The behaviour of elements and element ratios in melts during impregnation may be explained as follows.

- (1) Alkalis, Al₂O₃, and TiO₂ behave as incompatible elements and are concentrated in the melt as crystallization proceeds: their larger concentrations in the experimental melts compared with the initial gel compositions simply reflect the high melt consumption during the impregnation reaction. This effect is specially marked in run I16-15 owing to the small fraction of residual melt after equilibration (6.6%).
- (2) The behaviour of CaO in the melt is mainly controlled by the amount of Cpx precipitated in the impregnation reaction. Thus the constant CaO content in run I40-15 (compared with gel 40) is explained by the near-null participation of Cpx in the reaction [reaction (9a) below]. Conversely, the strong precipitation of Cpx in run I16-15 [reaction (10a) below] resulted in a major decrease of CaO in the residual melt (from 12.1 to 8.5%).
- (3) The strong silica enrichment in melt from runs I16-15 and I16-10 is due to Opx dissolution, Ol precipitation, and melt consumption during impregnation [reactions (10a) and (11) below]. In spite of this SiO₂ increase, the degree of silica undersaturation is larger in run I16-15 (8% normative Ne) than in gel 16 (5% normative Ne) owing to the significant increase of the alkali content in the melt (from 1.2 to 4.6%). In contrast, the melt in run I16-10 is Hy-normative (~10%), a feature that we relate to the smaller consumption of melt during the reaction and the consequent smaller alkali content in the melt (1.8%). In run I40-15, the silica content in the melt remains nearly constant, but the alkali content increases significantly; hence, the degree of silica undersaturation strongly increases (from 1% normative Ne in gel 40 to 17% in melt I40-15).
- (4) Mg-number increase is related to equilibration with peridotite (Mg-number = 90.7). Partial melts in equilibrium with a solid matrix rich in high-Mg-number Ol, such as mantle peridotites, have FeO contents that evolve within a narrow band at a given *P* owing to the olivine buffering effect (e.g. Kushiro, 1996; Médard *et al.*, 2006): from ~4 to 10.5% FeO at

1.5 GPa (Kushiro, 1996; Robinson *et al.*, 1998; Falloon & Danyushevsky, 2000). In comparison, the initial melts in our experiments are significantly enriched in FeO: 11.1% in gel 40 and 24.6% in gel 16. Hence, they underwent a major drop of FeO content during their equilibration with peridotite Bri2: from 11.1% in gel 40 to 7.0% in I40-15, and from 24.6% in gel 16 to 15.2% in I16-15. In contrast, their MgO content varied little during interaction with peridotite. Indeed, at a given temperature, melts from pyroxenites and from peridotites have similar MgO contents (Lambart *et al.*, 2009a).

Impregnation experiments: comparison with pMELTS calculations

The experimental phase proportions are compared with the proportions calculated with pMELTS in Table 6. The calculations were performed with the same starting compositions (Bri2, I40, and I16; Tables 1 and 3) and at the same pressure as in the experiments, but at a temperature 60°C higher than the experimental temperature (i.e. 1310°C vs 1250°C). This is to take into account the temperature shift between pMELTS predictions and the experimental data, as discussed by Ghiorso *et al.* (2002). The theoretical modes in Table 6 are slightly different from those for case 1 in Table 5 because the synthetic gels 40 and 16 do not exactly match the compositions of the pyroxenite-derived melts used in the thermodynamic approach (Tables 2 and 3). The differences are relatively small, however, compared with the modal changes owing to the impregnation reaction: in the Ol–Opx–Cpx triangle (Fig. 3a), the modes computed for bulk compositions I40 and I16 plot close to the modes obtained after impregnation of 100 g of peridotite Bri2 by 100 g of melt from pyroxenites M5-40 or M7-16.

As in the thermodynamic section above, phase abundances are given as masses, not as percentages: for run Bri2-15 (equilibration experiment on peridotite Bri2 at 1.5 GPa and 1250°C), we give the mass of each phase for 100 g of peridotite; for the three impregnation experiments, which simulate the equilibration of 100 g of peridotite with 100 g of melt, we give the mass of each phase for a bulk mass of 200 g. In this way, the behaviour of a phase is obvious: its mass increases if it is on the product side of the impregnation reaction, it decreases if it is on the reactant side, and the difference between its final mass in a 200 g bulk mass and its initial mass in 100 g of peridotite gives its coefficient in the impregnation reaction (written in grams for 100 g of added liquid). It should be noted that we can only write a global impregnation reaction corresponding to the addition of 100 g of melt: unlike with the thermodynamic approach, we cannot detect a switch in the impregnation reaction in relation to the exhaustion of

Table 6: Comparison between the modes measured in the impregnation experiments and the theoretical modes calculated with pMELTS

	Bri2-15		Gel 40	I40-15		Gel 16	I16-15		Bri2-10*	I16-10	
	exp	calc		exp	calc		exp	calc		exp	calc
ol	65.0	64.3		32.2	7.7		86.3	80.3	65.0	98.0	83.4
opx	21.7	24.4		85.4	104.1		0.3	—	23.7	0	0
cpx	13.1	10.5		13.3	25.5		93.1	106.5	7.1	19.0	32.2
sp	0.2	0.7		5.6	7.8		7.1	8.0	0.3	0.2	0
liq	—	—		63.5	54.9		13.3	5.1	3.8	82.7	84.3
a_{SiO_2} †			0.44	0.35		0.31	0.35				

Modes are given as masses, not percentages, and are expressed in two ways: for the initial states Bri2-15 (peridotite Bri2 at 1.5 GPa and 1250°C) and Bri2-10 (peridotite Bri2 at 1 GPa and 1250°C), we give the mass of each phase for 100 g of peridotite; for the final states I40-15, I16-15, and I16-10, which correspond to the equilibration of 100 g of peridotite with 100 g of melt, we give the mass of each phase for a bulk mass of 200 g. The calculations were performed at the same pressure as the experiments ($P=1.5$ GPa for Bri2-15, I40-15, and I16-15; $P=1$ GPa for Bri2-10 and I16-10), but at a temperature 60°C higher than the experimental temperature (1310°C vs 1250°C) to take into account the temperature shift between pMELTS predictions and experimental data (Ghiorso *et al.*, 2002). Oxygen fugacity was set to FMQ – 1 in all calculations.

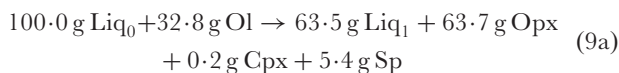
*As we did not run an experiment with peridotite Bri2 at 1 GPa and 1250°C, we give only the theoretical mode for the initial state Bri2-10.

†The impregnation reaction and thus the evolution of phase proportions are controlled by the silica activity, a_{SiO_2} , in the initial liquids (gel 40, gel 16). Silica activities were calculated using the MELTS supplemental calculator (Ghiorso & Sack, 1995; Asimow & Ghiorso, 1998) at 1.5 GPa and 1310°C.

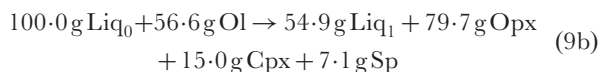
a solid phase and/or the precipitation of a new phase. As the solid phase assemblage in runs I40-15 and I16-15 is the same as in peridotite Bri2, this difficulty concerns only experiment I16-10 in which we do not know the mass of melt required to exhaust Opx.

The theoretical mode computed before impregnation is in good agreement with the mode measured in experiment Bri2-15: the masses calculated for Opx and Sp are overestimated and the mass of Cpx is underestimated, but they remain within the uncertainty of the mass-balance calculations in Table 4. The theoretical modes after impregnation are also consistent with those observed in experiments I40-15, I16-15, and I16-10, in spite of some systematic deviations (underestimation of Ol fraction and overestimation of Cpx and Sp fractions in the calculations). The comparison of the global impregnation reactions predicted by pMELTS with the reactions inferred from experimental data supports this agreement:

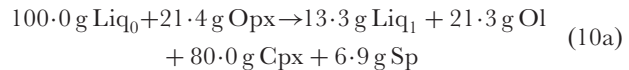
I40-15 (exp):



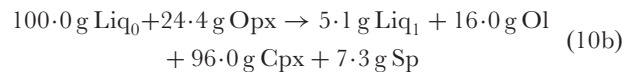
I40-15 (calc):



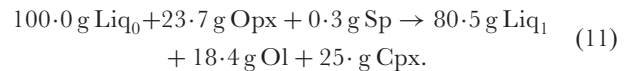
I16-15 (exp):



I16-15 (calc):



I16-10 (calc):



In the case of I16-10, we give only the thermodynamic impregnation reaction because we have no experimental constraints on the mode of peridotite Bri2 at 1 GPa and 1250°C.

In Fig. 6, we present the compositional difference between melts calculated with pMELTS and the experimental melts. This figure highlights that pMELTS significantly underestimates the CaO contents and overestimates the MgO and FeO contents of melts in comparison with the experimental melts. It should be noted that Na₂O is also significantly overestimated in calculations on I40-15 and I16-15. In the case of I16-10, on the contrary, Na₂O is slightly underestimated by pMELTS (1.33%) compared with the experiment (1.57%). These

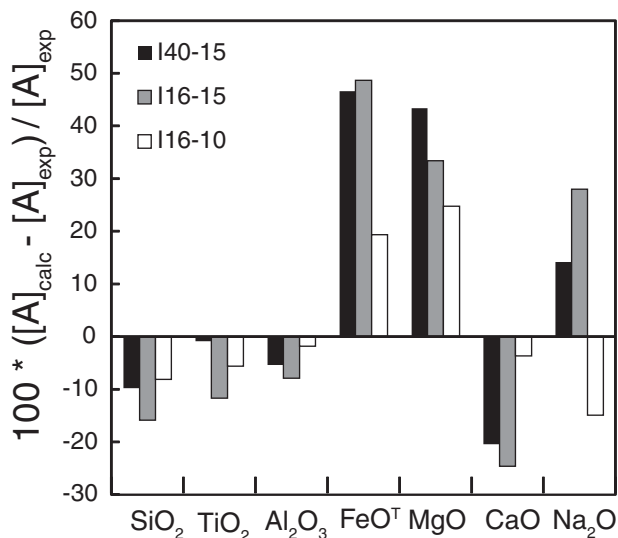


Fig. 6. Comparison between the melt compositions calculated with pMELTS and the melt compositions measured in experiments I40-15, I16-10, and I16-15. For each oxide A , the figure shows the relative difference between the calculated and the measured concentrations: $100(A_{\text{calc}} - A_{\text{exp}})/A_{\text{exp}}$. All iron is considered as Fe^{2+} (FeO^{T}).

discrepancies are due to the limitations of pMELTS as discussed by Ghiorso *et al.* (2002), and are consistent with the overestimation of Cpx production in the calculations compared with the experiments (see above), the much lower coefficients for the residual liquid in reactions (9b) and (10b) than in reactions (9a) and (10a) respectively, and the much larger Ol coefficient in reaction (9b) than in reaction (9a). Despite these differences, there is a perfect qualitative agreement between the thermodynamic and experimental approaches as the reactions predicted by pMELTS have the same form as those deduced from the experiments: the same phases are on the reactant side of the reactions (Ol for I40-15; Opx for I16-15) and on the product side (Opx, Cpx, and Sp for I40-15; Ol, Cpx, and Sp for I16-15). The agreement is also good quantitatively as in most cases the coefficients in the thermodynamic reactions are close to those in the experimental ones. In addition, it is possible that part of the difference between the melt fractions predicted by pMELTS and those measured in the experiments is linked to a small amount of dissolved volatiles in the experimental glasses. This hypothesis is supported by the case of I16-10: the experimental glass in I16-10 is presumably volatile-free as its analytical total is 99.9%, and this is the only case in which the quantity of melt measured in the experiment is equal (within error) to the quantity predicted by pMELTS.

We conclude that pMELTS is a reliable tool to estimate qualitatively and quantitatively the impregnation reactions between pyroxenitic melts and surrounding peridotite. In particular, the experimental study supports one of the

main conclusions of the thermodynamic study (for cases 1 and 2): melts from pyroxenites are strongly consumed by interaction with subsolidus peridotite (Fig. 2), a factor that should tend to limit further melt infiltration and to isolate the pyroxenite bodies from the surrounding peridotites.

DISCUSSION AND PETROLOGICAL IMPLICATIONS

Synthesis of thermodynamic and experimental results

Four major results emerge from our calculations and experiments on the impregnation of subsolidus peridotites by pyroxenite-derived melts (cases 1 and 2): the massive production of clinopyroxene, the contrasted behaviour of Opx and Ol depending on the composition of the added melt, the transformation of lherzolites into Ol websterites or wehrlites, and the important consumption of the added melt. A fifth result comes from our calculations on case 3; namely, the minor effect of pyroxenitic melts on partially molten peridotites at low pressure. These results are summarized below.

- (1) Massive production of clinopyroxene. As a rule, large amounts of Cpx (and small quantities of Sp at 1.5 GPa or Gt at 2.5 GPa) are produced during the impregnation of subsolidus peridotites by pyroxenite-derived melts at 1.5–2.5 GPa. In the most extreme cases, the mass of pyroxene produced is larger than the mass of added liquid: for instance, 1.15 g of Cpx per gram of added liquid in reaction (3a).
- (2) Contrasted behaviours of Ol and Opx. Both calculations and experiments show that the behaviours of Ol and Opx depend on the composition of the added liquid. In the case of melt from pyroxenite M5-40, Opx is on the product side of the impregnation reaction and Ol on the reactant side, at both 1.5 and 2.5 GPa [reactions (2), (4), (9a) and (9b)]. Conversely, in the case of melt from M7-16, Ol is on the product side and Opx on the reactant side [reactions (3a), (5a), (10a) and (10b)]. In the next section, we show that the main factor controlling the behaviour of Ol and Opx during peridotite–pyroxenite interactions is the silica activity of the infiltrating melt, not its degree of silica undersaturation as the liquids from M7-16 and M5-40 have similar percentages of normative nepheline (Table 2).
- (3) Fate of pyroxenite-derived melts in a subsolidus environment. All impregnation reactions at 1.5 and 2.5 GPa are accompanied by an important consumption of pyroxenitic melt: from ~35–45% [reactions (4), (9a) and (9b)] to ~85–100% [reactions (3a), (10a) and (10b)] of the added melt is lost during the equilibration with peridotite. In particular, we observe that reactions (3a), (5a), (10a) and (10b), which

have Ol on the product side, yield only very little residual liquid owing to the massive precipitation of Cpx. Hence, in our experiments and calculations for cases 1 and 2, peridotite–pyroxenite interactions tend to consume a significant fraction of the liquids produced by the partial melting of pyroxenites and to precipitate large quantities of pyroxenes. These effects are expected to decrease drastically the permeability of the system and the capacity of pyroxenite-derived melts to infiltrate neighbouring rocks.

- (4) From lherzolites to Ol websterites or wehrlites. The impregnation process results in major changes of the modal composition of the solid assemblage (Fig. 3a and b). In the case of melts from M5-40, the solid assemblage goes from the lherzolite field to the Ol websterite field owing to the precipitation of Opx and Cpx, and the dissolution of Ol. In the case of the melts from M7-16, the evolution is from the lherzolite field toward the wehrlite field owing to the precipitation of Cpx and the dissolution of Opx.
- (5) Minor effect of peridotite–pyroxenite interactions at low pressure. Lambart *et al.* (2009a) showed that many pyroxenites produce liquids that are similar to peridotite-derived melts for most major elements (SiO₂, Al₂O₃, CaO, MgO, and FeO) at 1 GPa and 1250–1300°C. Accordingly, a restricted effect of the impregnation by pyroxenite-derived melts may be the rule for most pyroxenites at the *P–T* conditions corresponding to our case 3, as we observed for the melt derived from M5-40. In particular, we want to emphasize that for both pyroxenites M5-40 and M7-16, the mass of residual liquid is close to the mass of added liquid [reactions (6), (7a) and (7b)]; that is, only a small fraction of the added liquid is consumed during the impregnation process. This behaviour is the opposite of that observed in cases 1 and 2 above. Hence, in the conditions of case 3, the impregnation process will not ‘clog’ the melt pathways in the peridotite. This result suggests that when the overlying peridotites are partially molten, the pyroxenitic melt can be extracted and percolate from its source through the mantle.

Factors controlling the dissolution or precipitation of Ol and Opx

In many theoretical (e.g. Lundstrom *et al.*, 2000; Kogiso *et al.*, 2004b), experimental (e.g. Keshav *et al.*, 2004; Kogiso & Hirschmann, 2006) and petrological (e.g. Griffin *et al.*, 1999; Aulbach *et al.*, 2007; Piccardo & Vissers, 2007) studies, it is assumed that a silica-undersaturated melt interacting with peridotite consistently dissolves pyroxenes and precipitates Ol. The liquid from pyroxenite M7-16, which is Ne-normative (Table 2), does

indeed dissolve the Opx from peridotite Bri2 and precipitate Ol. However, the liquid from pyroxenite M5-40, which is also silica-undersaturated and Ne-normative (Table 2), dissolves Ol and precipitates Opx. In fact, the melts from pyroxenites M5-40 and M7-16 have similar percentages of normative Ne (from 6 to 9%; Table 2), but contrasted silica contents: the melt from M5-40 contains 50.6% SiO₂ at 1.5 GPa and 48.7% at 2.5 GPa whereas the melt from M7-16 contains 41.6% SiO₂ at 1.5 GPa and 39.1% at 2.5 GPa. Accordingly, the main factor controlling the behaviour of Ol and Opx during peridotite–pyroxenite interactions is the silica content of the infiltrating melt, or more strictly the silica activity, not the degree of silica undersaturation.

In most impregnation calculations, the liquid is in equilibrium with a lherzolitic assemblage: Ol + Opx + Cpx + Sp/Gt (except after Opx exhaustion; Fig. 2). The silica activity of Ol + Opx-saturated melts, $a_{\text{SiO}_2}^0$, is buffered by the reaction $\text{Ol} + (\text{SiO}_2)_{\text{liquid}} \leftrightarrow 2 \text{Opx}$. Therefore, at fixed temperature and pressure, $a_{\text{SiO}_2}^0$ will be nearly constant, even though liquid compositions may vary considerably (Carmichael *et al.*, 1970). Hence, in an interaction process at constant *P* and *T* as described in this paper, the silica activity of the added melt will condition the behaviour of Opx and Ol during the reaction: if the added liquid has a silica activity lower than $a_{\text{SiO}_2}^0$, which is the case of the melts from M7-16 (see below), it will dissolve Opx and precipitate Ol until its silica activity equals $a_{\text{SiO}_2}^0$ (or until Opx exhaustion). If the added melt has a silica activity higher than $a_{\text{SiO}_2}^0$, which is the case of the melts from M5-40, then it will dissolve Ol and precipitate Opx until its silica activity equals $a_{\text{SiO}_2}^0$ (or Ol is exhausted).

To illustrate this point, we computed the silica activities in melts from experiments I40-15 and I16-15, and in initial melts gel 40 and gel 16 (silica activities were calculated using the MELTS supplemental calculator; see Table 6). As expected, liquids from runs I40-15 and I16-15, which are both in equilibrium with Ol + Opx (+ Cpx + Sp), have similar silica activities: ~0.35. In contrast, silica activities in the initial melts are different: 0.44 in gel 40 vs 0.31 in gel 16. These calculations confirm the major control exerted by silica activity on the impregnation reaction: impregnation of peridotite by a melt with a low silica activity, such as gel 16, leads to Opx dissolution and Ol precipitation, while impregnation by a liquid with a high silica activity, such as gel 40, results in Ol dissolution and Opx precipitation.

To highlight the relationship between silica activity, the evolution of melt compositions and phase relations during melt–rock interactions, melt compositions at the beginning (gels 16 and 40) and at the end (experimental glasses in runs I16-15 and I40-15) of the impregnation process at 1.5 GPa are projected from diopside (Di) onto the

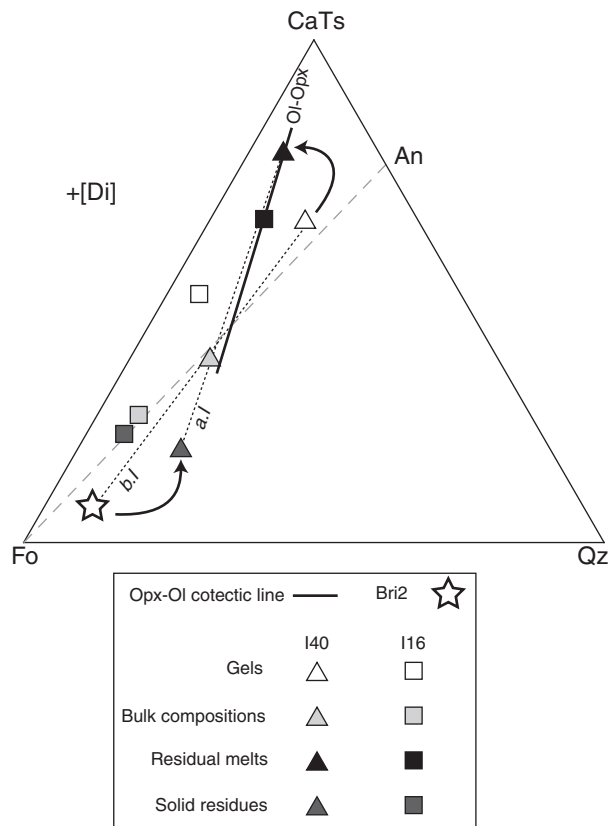


Fig. 7. Molar projections from diopside [Di] onto the pseudo-ternary diagram forsterite–calcium Tschermak pyroxene–quartz [Fo–CaTs–Qz] ($\text{CaAl}_2\text{SiO}_6$ –Qz) of starting materials and products of impregnation experiments at 1.5 GPa, I40–I5 and I16–I5. The bold straight line represents the Ol–Opx cotectic line at 1.5 GPa defined by straight line in equilibrium with Opx and Ol in our experiments at 1.5 GPa. The dashed line is the forsterite–anorthite (An) join, which separates Ne- from Hy-normative compositions in this projection. Symbols are as follows: triangles, experiment on pyroxenite M5-40 (I40–I5); squares, experiments on pyroxenite M7-16 (I16–I5); star, peridotite Bri2. White symbols are for starting end-members (gels 16 and 40, and peridotite Bri2), light grey ones for bulk compositions I40 and I16, dark grey and black ones for solid residues and melts, respectively, in experiments I40–I5, and I16–I5. The tie lines join solid and liquid before (b.I) and after (a.I) the equilibration of Bri2 with gel40 and arrows illustrate the rotation of the solid–liquid tie line around the bulk composition during the equilibration process.

forsterite–calcium Tschermak pyroxene–quartz (Fo–CaTs–Qz) plane (Fig. 7). In this representation, the experimental glasses in runs I40–I5 and I16–I5, which are saturated with Ol and Opx (with a silica activity equal to $a_{\text{SiO}_2}^0$), are on the 1.5 GPa Ol–Opx cotectic line. In contrast, melts with $a_{\text{SiO}_2} > a_{\text{SiO}_2}^0$ (such as gel 40) plot on the right side of the cotectic, and melts with $a_{\text{SiO}_2} < a_{\text{SiO}_2}^0$ (such as gel 16) plot on the left side. Pyroxenite melt compositions that are located within the triangle bounded by the Ol–Opx cotectic on the left and by the Fo–An join on the right, are Ne-normative, but yet will dissolve Ol during peridotite impregnation.

Figure 7 allows us to display the evolution of the liquid phase and of its solid matrix (the ‘residue’) during the impregnation experiments. Runs I40–I5 and I16–I5 show the same behaviour for CaTs and Fo (with an enrichment in CaTs and a depletion in Fo in both the liquid and the solid residue) but a contrasted behaviour for Qz. To attain the Ol–Opx cotectic, the liquid in run I40–I5 must become poorer in the Qz component through Ol dissolution and Opx precipitation; in parallel, the solid residue becomes richer. As a result, the tie line joining the solid and the liquid and passing through the bulk composition rotates anticlockwise during the equilibration process (arrows in Fig. 7). The relationships are exactly the reverse in the case of experiment I16–I5: the liquid must become richer in Qz to reach the Ol–Opx cotectic, the solid residue becomes poorer and this is achieved by Opx dissolution and Ol precipitation.

Implications for the lithological diversity of the upper mantle: the case of Ronda

Our calculations and experiments show that the interaction between melts derived from pyroxenites and surrounding rocks in a heterogeneous mantle may generate new rock-types, including cpx-rich peridotites, wehrlites and ol-websterites (Fig. 3). In this section, we show that the ultramafic massif of Ronda, SW Spain, provides a natural example where a new generation of pyroxenites was produced by interactions between peridotites and percolating melts derived from older pyroxenites. Ronda pyroxenites are divided into four groups (A–D; Garrido & Bodinier, 1999), of which groups A and C are of special interest for our study. Pyroxenites from group A are mainly Gt pyroxenites with a strong radiogenic Os isotopic signature whereas group C pyroxenites are Sp-bearing websterites and Ol websterites with $^{187}\text{Os}/^{186}\text{Os}$ ratios intermediate between group A pyroxenites and the surrounding peridotites (Reisberg *et al.*, 1991). On the basis of petrological and geochemical observations, Garrido & Bodinier (1999) proposed a model in which group C pyroxenites were produced by interactions between the surrounding peridotites and a reacting melt with a component derived from the partial melting of group A pyroxenites; the latter component has high $^{187}\text{Os}/^{186}\text{Os}$ ratios. We compared the modal proportions of Ol, Opx, and Cpx in group C pyroxenites with those predicted by pMELTS for our case 1 (Fig. 3a); it should be noted that the P – T conditions of case 1 (1250°C and 1.5 GPa) are close to those estimated for the thermal event in Ronda: $T \geq 1200^\circ\text{C}$, $P \approx 1.5$ GPa (Lenoir *et al.*, 2001). Group C pyroxenites have modes consistent with the impregnation of peridotite by melts with compositions close to the melt from M5-40 or intermediate between melts from M5-40 and M7-16 at 1.5 GPa and 1250°C: melts with a high silica activity, such as the melt from M5-40, are good candidates to generate the most Opx-rich websterites (with Opx/Cpx ratios approaching

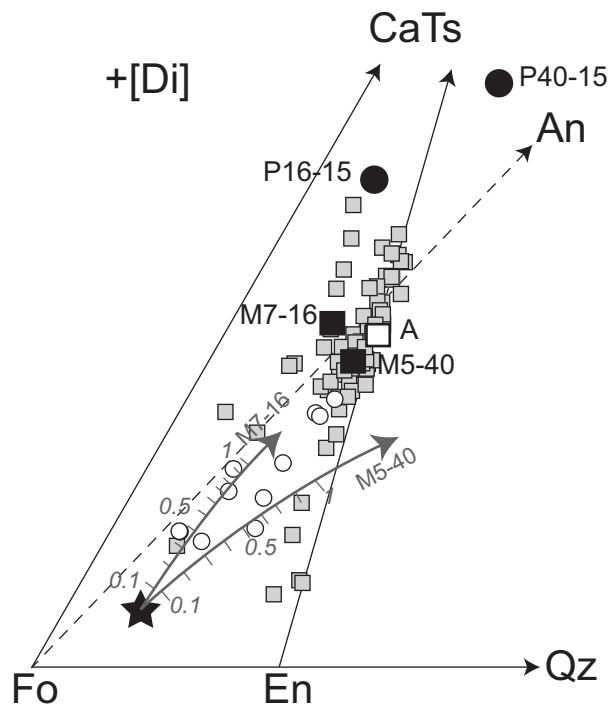


Fig. 8. Molar projections from diopside [Di] onto the pseudo-ternary diagram forsterite–calcium Tschermak pyroxene–quartz (Fo–CaTs–Qz) of group C pyroxenites from the Ronda massif (white circles; Bodinier *et al.*, 2008), of the mean composition of group A pyroxenites from Ronda (white square; Garrido & Bodinier, 1999), of pyroxenites from the Beni Bousera massif (grey squares; Kornprobst, 1970; Pearson *et al.*, 1993; Kumar *et al.*, 1996), of pyroxenites M5-40 and M7-16 (black squares), and of their melts at 15 GPa and 1250°C (P40-15 and P16-15, respectively; black circles). Arrows labelled ‘M5-40’ and ‘M7-16’ display the compositional trends calculated with pMELTS for the residual solids of peridotites impregnated by liquids P40-15 and P16-15; arrow ticks correspond to the scale of magma/rock ratios from 0.1 to 1. The composition of peridotite Bri2 before impregnation is represented by the black star. En, enstatite; An, anorthite.

2); melts with a lower silica activity are required to produce less Opx and to yield Opx/Cpx ratios close to 1 as in most group C websterites. In Fig. 8, compositions of group C pyroxenites are projected from Di onto the Fo–CaTs–Qz plane and are compared with pyroxenites from the Beni Bousera massif (Kornprobst, 1970; Pearson *et al.*, 1993; Kumar *et al.*, 1996). This figure shows that group C pyroxenites are enriched in the Fo component compared with most pyroxenites from Beni Bousera. Moreover, it confirms that the impregnation of a peridotite by melts intermediate between partial melts from M5-40 and M7-16 at 15 GPa and 1250°C may well reproduce the compositions of group C pyroxenites (we observe the same relations with the projection from CaTs onto the Fo–Di–Qz plane). Additionally, we note that, for many major elements (SiO₂, FeO, MgO, CaO and Na₂O), the mean composition of group A pyroxenites from Ronda is intermediate

between M5-40 and M7-16 (though closer to M5-40; Table 1, Fig. 8). Accordingly, the conclusion that partial melts derived from group A pyroxenites are a major component of the mixture of melts that reacted with peridotite to yield group C pyroxenites (Garrido & Bodinier, 1999) is supported by our study. Finally, based on trace element distribution in Cpx, Bodinier *et al.* (2008) estimated that the magma/rock ratio required to produce group C pyroxenites is between 0.5 and 1.7. These estimations agree with those inferred from our calculations: ≥ 0.4 for Ol websterites and significantly greater than 1 for true websterites (Figs 3a and 8).

As a whole, there is a good qualitative and quantitative agreement between the petrological and geochemical studies of Bodinier and collaborators and the present sets of calculations and experiments. We conclude that interactions between percolating melts, especially those derived from pyroxenites, and host peridotites can increase the lithological and compositional diversity of the mantle, and produce new types and generations of peridotites and pyroxenites (for instance, peridotites with less than 50% Ol and/or low Mg-number, or websterites with a high Opx/Cpx ratio). It should be noted that this type of process is also likely to occur in the source regions of basalts. Indeed, the formation of pyroxenite via liquid–rock interactions has recently been proposed to explain the compositions of oceanic basalts (e.g. Sobolev *et al.*, 2007) and the origin of iron-rich peridotites (e.g. Tommasi *et al.*, 2004).

Implications for the extraction and transport of pyroxenite partial melts at high pressure

The solidus temperatures of pyroxenites are lower than those of peridotites: accordingly, pyroxenites begin to melt deeper than peridotites in a heterogeneous mantle ascending adiabatically. In addition, Gt remains stable at lower pressures in pyroxenites than in peridotites. These properties were used by Hirschmann & Stolper (1996) to model magma genesis at mid-ocean ridges and to reinterpret the garnet signature in MORB: if bodies of pyroxenite are present in the ascending mantle, then melts with a garnet signature (i.e. with compositions indicating the presence of residual Gt in the source region, such as a high LREE/HREE or a decoupling of Hf–Nd isotope systematics) can be produced at lower pressures than in the case of a homogeneous peridotitic mantle. If we admit that the trace-element garnet signature in MORB is supplied by pyroxenite-derived melts, then the reaction between melts once in equilibrium with Cpx + Gt and the surrounding peridotite must be limited, so that they can preserve their geochemical characteristics en route to the surface. We discuss below the case of isolated pyroxenite bodies in a peridotite matrix and the mechanisms that would allow the

extraction and transport of pyroxenite-derived melt with minimal interactions with the peridotite.

Pyroxenite bodies in a subsolidus mantle

At high pressure, between the pyroxenite solidus and the peridotite solidus, the melting degree of pyroxenites is low to moderate while the surrounding peridotites are unmolten (case 2 in Table 2; the considerations below also apply if the peridotite crosses its solidus as long as its degree of melting remains very low). Interactions at the peridotite–pyroxenite interface result in the consumption of a large part of the pyroxenite-derived melt and the crystallization of Cpx + Gt + Opx or Cpx + Gt + Ol (depending on pyroxenite composition; Fig. 2c and d). Hence, a low-permeability layer develops around the pyroxenite body, favouring a (near) closed-system evolution. In this context, gravity-driven solid–liquid separation could lead to the formation of melt-rich lenses at the top of the pyroxenite bodies. As such accumulations are mechanically unstable, the next step in the evolution of the system could be the periodic expulsion of melt into veins or channels (Kogiso *et al.*, 2004b), allowing the rapid transport of pyroxenite-derived melts to the surface and the preservation of their garnet signature.

Pyroxenite bodies surrounded by partially molten peridotite

Now we assume that the peridotite is partially molten and that its permeability is sufficiently large to allow the percolation of pyroxenite-derived melts. This situation is similar to our case 3 in Table 2, and corresponds to pressures close to the mean pressures of melting beneath mid-ocean ridges (1–1.5 GPa; e.g. Langmuir *et al.*, 1992). At these conditions, pyroxenites have high to very high degrees of melting and many of them (such as M5-40) yield partial melts that are similar to peridotite-derived melts for most major elements (see Fig. 6 in Lambart *et al.*, 2009a). This small compositional contrast results in a very limited reactivity between pyroxenite-derived melt and peridotite [reaction (6); Figs 2e and 3c] that is favourable to the preservation of their trace element signature.

Special pyroxenite compositions such as M7-16

Lambart *et al.* (2009a) showed that, at a given pressure, pyroxenite partial melts may have strongly contrasted silica contents depending on whether they are saturated in Opx or not. In particular, low-SiO₂ clinopyroxenites such as M7-16 produce liquids that are strongly depleted in SiO₂ in comparison with peridotite-derived melts. Our calculations and experiments indicate that interaction between such low-SiO₂ melts and the surrounding peridotite leads to Opx dissolution [reactions (3), (5), (7), (10a) and (10b)] and formation of wehrlite or Opx-free clinopyroxenite as solid residues (Fig. 3). At low pressure (1–1.5 GPa), when peridotites are partially molten (our case 3), melt consumption is limited [~10% in reaction (7); Fig. 2f],

and thus low-SiO₂ pyroxenite-derived melts can be extracted from their source. However, as they are very different from typical peridotite melts, they will interact with the surrounding peridotite and undergo significant chemical changes, as exemplified by gel 16 in experiment I16-10 (Tables 3 and 4). In particular, a strong enrichment in silica of the percolating melt, associated with Opx dissolution in the solid matrix, is expected, to increase its silica activity and to approach the Ol–Opx cotectic, as discussed above (Fig. 7). Moreover, if pyroxenite-derived melts are enriched in iron compared with peridotite partial melts, they will also become depleted in iron. The importance of these chemical changes will decrease with additional melt infiltration because Opx and then Cpx will disappear from the solid matrix, leaving a pure Ol residue. Opx is expected to be rapidly exhausted (at a melt–rock ratio between 0.5 and 0.65 in our calculations). Extending our calculations in Fig. 2f to high melt/rock ratios, we computed that a ratio of ~8 is needed to exhaust Cpx. As pMELTS overestimates pyroxene production at the expense of Ol, the true melt–rock ratio required for Cpx exhaustion is probably much lower. Hence, pyroxene-free dunite regions could be formed by circulation and focusing of SiO₂-poor pyroxenitic melts within peridotite. Such melts could therefore contribute to the initiation and formation of a large-scale network of dunite channels, although their role is probably limited by the small proportion of low-SiO₂ pyroxenites in the upper mantle. Once a dunite network is established, additional melt could circulate without significant compositional change (Kelemen *et al.*, 1995).

A sketch of MORB petrogenesis in a heterogeneous mantle

The main conclusions of our study are summarized in Fig. 9. The conceptual model presented here does not take many dynamic parameters into account (such as the solid flow rate or the rate of melt extraction relative to the rate of matrix melting). However, it illustrates how our results can be applied to the natural case, summarizing (1) the effect of melt–peridotite interactions on melt transport and mantle lithological diversity, and (2) the role of pyroxenites in magma genesis at mid-ocean ridges (MOR). In Fig. 9, we consider a heterogeneous mantle made of veins of pyroxenite within a peridotitic matrix. As mantle ascends adiabatically beneath a MOR, it first crosses the pyroxenite solidus at high pressure: at this point, the pyroxenites give rise to Ne-normative liquids, which react with the surrounding peridotite (still subsolidus) to produce new rock-types (Gt-bearing hybrids intermediate between peridotites and pyroxenites). As peridotite–pyroxenite interactions consume a large fraction of the pyroxenite-derived liquids, they tend to stop further melt infiltration and to isolate the pyroxenite bodies from their host. At this stage, solid–liquid separation can lead to the

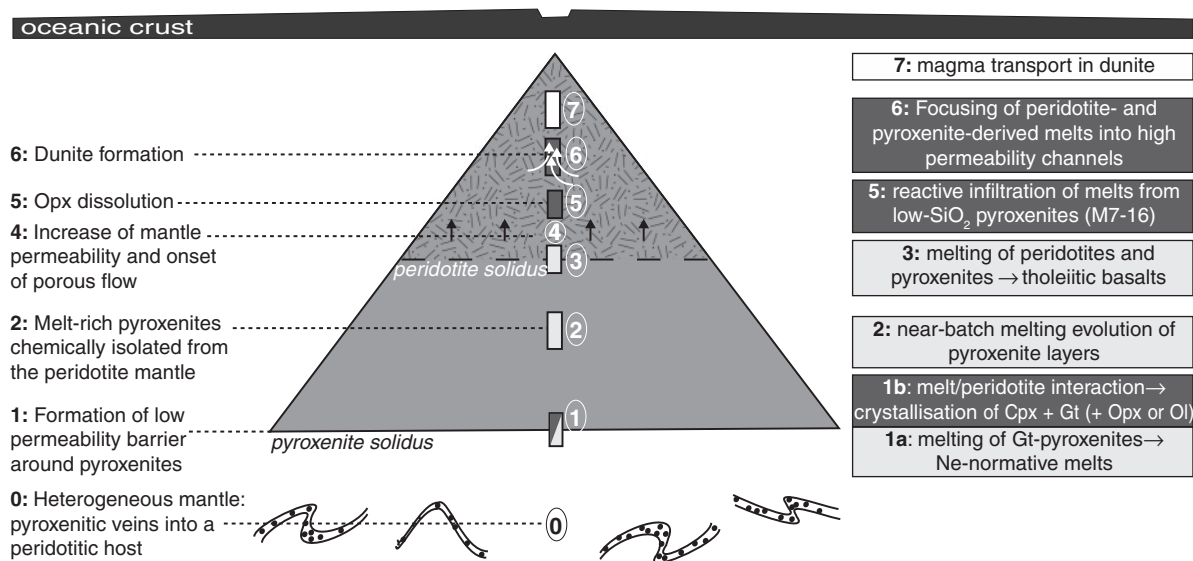


Fig. 9. Sketch of MORB petrogenesis in the case of a heterogeneous mantle composed of pyroxenite veins (dotted, folded layers at the bottom) in a peridotite matrix (see text). Processes acting at a given depth are listed in the boxes on the right: melting processes in light grey boxes, and peridotite–pyroxenite interactions in dark grey boxes. The outcome of each process for the chemical and mineralogical evolution of mantle is summarized in the left column. The grey triangle is the melting zone: in its lower part, only pyroxenites are partially molten; in its upper part (cross-hatched area), both pyroxenites and peridotites are partially molten. Black arrows above the peridotite solidus mark the onset of penetrative porous flow; white arrows represent melt focusing into high-permeability channels.

accumulation of melt-rich lenses at the top of the pyroxenite bodies, a situation favourable to the expulsion and rapid transport to the surface of melts carrying the geochemical signature of garnet. At some lower pressure (which depends on the local potential temperature of the mantle), the ascending mantle crosses the peridotite solidus, and an interconnected network of melt develops at the grain scale in the peridotite matrix. Rapidly, peridotite- and pyroxenite-derived melts begin to migrate upwards by diffuse porous flow. Most pyroxenite-derived melts should be able to percolate through the peridotite matrix with minimum interactions, thus preserving their isotopic and trace element signature. Because of their low silica activity, some pyroxenitic melts will, however, react with the peridotite and dissolve away Opx and possibly Cpx, a process that may initiate the formation of dunites and lead to a switch from pervasive porous flow to focused transport into a network of high-permeability dunite channels (Kelemen *et al.*, 1995). Such dunite channels provide the magma with a rapid pathway to the surface and a chemical isolation from the surrounding mantle, thus promoting the preservation of information about the melting process at depth (e.g. melting conditions, primary melt compositions, etc.).

Finally, we come back to processes of magma transport beneath MORs. The available geochemical data (e.g. O'Hara, 1968; Stolper, 1980; Johnson *et al.*, 1990) are explained by the fact that the migration of mantle melts

beneath a MOR occurs through focused flow along chemically isolated dunite channels (Kelemen *et al.*, 1997). However, the transition from diffuse porous flow to focused flow in channels remains unclear. The following models have been proposed to explain melt focusing: (1) formation of self-organized dissolution channels by reactive infiltration instability (e.g. Daines & Kohlstedt, 1994; Spiegelman *et al.*, 2001); (2) dike formation by hydraulic fracturing (e.g. Sleep, 1988; Takahashi, 1992); (3) mechanical stress-driven localization of melt (Holtzman *et al.*, 2003); (4) presence of a barrier to upward melt migration at the base of the oceanic lithosphere (e.g. Sparks & Parmentier, 1991; Ghods & Arkani-Hamed, 2000; Katz *et al.*, 2006). As a variant of (4), we propose that some mantle heterogeneities may evolve into permeability barriers able to trigger melt focusing. A body of partially molten pyroxenite isolated in the subsolidus peridotitic mantle could differentiate into a melt lens at the top and a layer of strongly compacted cumulates at the bottom. If the body is wide enough (>100 m; e.g. Spiegelman *et al.*, 2001), it could form a barrier to melt ascension, forcing the melt to focus along its sides. This assumption needs to be further studied and quantified, but could provide a viable mechanism for the onset of focusing. This is consistent with some previous studies: permeability barriers (Herbert & Montési, 2010) and compaction of the solid matrix (e.g. Spiegelman *et al.*, 2001) are two factors that can promote melt focusing.

CONCLUSIONS

To predict the fate of pyroxenite-derived melts during their migration through the peridotitic mantle, we performed a thermodynamic (with pMELTS) and experimental study of the impregnation of a peridotite by pyroxenite-derived melts. Three contexts were considered: (1) in a subsolidus lithospheric mantle; (2) at high pressure beneath a mid-ocean ridge, in a subsolidus asthenospheric mantle; (3) at lower pressure beneath a mid-ocean ridge, in a partially molten asthenospheric mantle.

Despite some mismatches observed between model outputs and observations (Cpx overestimation, temperature offset) showing that pMELTS still needs to be improved, our work shows that the software is a suitable tool to estimate qualitatively the impregnation reactions between pyroxenitic melts and surrounding peridotite.

More importantly, this study highlights the importance of magma–rock interactions for MORB petrogenesis and for the development of mantle lithological diversity, and, in particular, their significant impact on magma extraction processes. Reactions are varied—they depend on many parameters such as melt composition, pressure and the melting degree of surrounding rock—and experimental data are still too sparse. The scientific challenge is now to successfully incorporate these processes into a dynamic melting model of a heterogeneous mantle.

ACKNOWLEDGEMENTS

The authors are grateful to Jacques Kornprobst, Emeritus Professor at Université Blaise Pascal, Clermont-Ferrand, for providing the two pyroxenites from Beni Bousera used in this study. This study has benefited from discussions with Michel Pichavant, Othmar Müntener, Etienne Médard and Muriel Laubier. Special thanks are due to the following persons: Jean-Louis Fruquière and Frank Pointud for manufacturing the piston-cylinder assemblages and for maintenance operations; Jean-Luc Devidal for technical assistance with the electron microprobe and for the preparation of synthetic gels; Jean-Marc Hénot for technical assistance with the scanning electron microscope; Mhammed Benbakkar for the ICP-AES analyses of pyroxenites and synthetic gels. We also thank Tetsu Kogiso, Bruno Scaillet and an anonymous reviewer for their constructive reviews.

FUNDING

This work was supported by the program DyETI of the Institut National des Sciences de l'Univers (INSU-CNRS) and by the Agence Nationale de la Recherche 'MIME' grant (ANR-07-BLAN-0130-01 to A.P.).

REFERENCES

- Albarède, F. & Provost, A. (1977). Petrological and geochemical mass-balance equations: an algorithm for least-square fitting and general error analysis. *Computers and Geosciences* **3**(2), 309–326.
- Allègre, C. J. & Turcotte, D. L. (1986). Implications of a two-component marble-cake mantle. *Nature* **323**(6084), 123–127.
- Ancey, M., Bastenaire, F. & Tixier, R. (1978). Application des méthodes statistiques en microanalyse. In: Maurice, F., Meny, L. & Tixier, R. (eds) *Microanalyse, microscopie à balayage*. Orsay: Les éditions du physicien, pp. 323–347.
- Asimow, P. D. & Ghiorso, M. S. (1998). Algorithmic modifications extending MELTS to calculate subsolidus phase relations. *American Mineralogist* **83**, 1127–1132.
- Asimow, P. D., Hirschmann, M. M., Ghiorso, M. S., O'Hara, M. J. & Stolper, E. M. (1995). The effect of pressure-induced solid–solid phase transitions on decompression melting of the mantle. *Geochimica et Cosmochimica Acta* **59**(21), 4489–4506.
- Aulbach, S., Griffin, W. L., Pearson, N. J., O'Reilly, S. Y. & Doyle, B. J. (2007). Lithosphere formation in the central Slave Craton (Canada): plume subcretion or lithosphere accretion? *Contributions to Mineralogy and Petrology* **154**, 409–427.
- Baker, M. B. & Stolper, E. M. (1994). Determining the composition of high-pressure mantle melts using diamond aggregates. *Geochimica et Cosmochimica Acta* **58**(13), 2811–2827.
- Berman, R. G. & Koziol, A. M. (1991). Ternary excess properties of grossular–pyrope–almandine garnet and their influence in geothermobarometry. *American Mineralogist* **76**, 1223–1231.
- Bodinier, J.-L., Garrido, C. J., Chanéfo, I., Brugruier, O. & Gervilla, F. (2008). Origin of pyroxenite–peridotite veined mantle by refertilization reactions: evidence from the Ronda peridotite (Southern Spain). *Journal of Petrology* **49**(5), 999–1025.
- Carmichael, I. S. E., Nicholls, J. & Smith, A. L. (1970). Silica activity in igneous rocks. *American Mineralogist* **55**, 246–263.
- Christie, D. M., Carmichael, I. S. E. & Langmuir, C. H. (1986). Oxidation states of mid-ocean ridge basalt glasses. *Earth and Planetary Science Letters* **79**, 397–311.
- Cottrell, E. & Kelley, K. A. (2011). The oxidation state of Fe in MORB glasses and the oxygen fugacity of the upper mantle. *Earth and Planetary Science Letters* **305**, 270–282.
- Daines, M. J. & Kohlstedt, D. L. (1994). The transition from porous to channelized flow due to melt/rock reaction during melt migration. *Geochemistry, Geophysics, Geosystems* **21**(2), 145–148.
- Dick, H. J. B. & Sinton, J. M. (1979). Compositional layering in Alpine peridotites: evidence for pressure solution creep in the mantle. *Journal of Geology* **87**, 403–416.
- Falloon, T. J. & Danyushevsky, L. V. (2000). Melting of refractory mantle at 1.5, 2 and 2.5 GPa under anhydrous and H₂O-undersaturated conditions: implications for the petrogenesis of high-Ca boninites and the influence of subduction components on mantle melting. *Journal of Petrology* **41**(2), 257–283.
- Faul, U. H. (1997). Permeability of partially molten upper mantle rocks from experiments and percolation theory. *Journal of Geophysical Research* **102**(B5), 10299–10311.
- Garrido, C. J. & Bodinier, J.-L. (1999). Diversity of mafic rocks in the Ronda peridotite: Evidence for pervasive melt–rock reaction during heating of subcontinental lithosphere by upwelling asthenosphere. *Journal of Petrology* **40**, 729–754.
- Ghiorso, M. S. & Sack, R. O. (1995). Chemical mass transfer in magmatic processes IV. A revised and internally consistent thermodynamic model for the interpolation and extrapolation of liquid–solid equilibria in magmatic systems at elevated temperatures and pressures. *Contributions to Mineralogy and Petrology* **119**(2), 197–212.

- Ghiorso, M. S., Hirschmann, M. M., Reiners, P. W. & Kress, V. C., III (2002). The pMELTS: A revision of MELTS for improved calculation of phase relations and major element partitioning related to partial melting of the mantle to 3 GPa. *Geochemistry, Geophysics, Geosystems* **3**(5), doi:10.1029/2001GC000217.
- Ghods, A. & Arkani-Hamed, J. (2000). Melt migration beneath MORs. *Geophysical Journal International* **140**, 687–697.
- Griffin, W. L., O'Reilly, S. Y. & Ryan, C. G. (1999). The composition and origin of subcontinental lithospheric mantle. In: Fei, Y., Bertka, C. M. & Mysen, B. O. (eds) *Mantle Petrology: Field Observations and High-pressure Experimentation*. *Geochemical Society Special Publications* **6**, 13–45.
- Herbert, L. B. & Montési, L. G. J. (2010). Generation of permeability barriers during melt extraction at mid-ocean ridges. *Geochemistry, Geophysics, Geosystems* **11**(12), doi:10.1029/2010GC003270.
- Herzberg, C., Asimow, P. D., Arndt, N., Niu, Y., Leshner, C. M., Fitton, J. G., Cheadle, M. J. & Saunders, A. D. (2007). Temperature in ambient mantle and plumes: Constraints from basalts, picrites and komatiites. *Geochemistry, Geophysics, Geosystems* **8**(2), doi:10.1029/2006GC001390.
- Hirschmann, M. M. & Stolper, E. M. (1996). A possible role for garnet pyroxenite in the origin of the 'garnet signature' in MORB. *Contributions to Mineralogy and Petrology* **124**(2), 185–208.
- Hirschmann, M. M., Ghiorso, M. S., Davis, F. A., Gordon, S. M., Mukherjee, S., Grove, T. L., Krawczynski, M., Medard, E. & Till, C. B. (2008). Library of experimental phase relations (LEPR): A database and Web portal for experimental magmatic phase equilibria data. *Geochemistry, Geophysics, Geosystems* **9**(3), doi:10.1029/2007GC001894.
- Holtzman, B. K., Groebner, N. J., Zimmerman, M. E. & Ginsberg, S. B. (2003). Stress-driven melt segregation in partially molten rocks. *Geochemistry, Geophysics, Geosystems* **4**(5), doi:10.1029/2001GC00258.
- Johnson, K. T. M., Dick, H. J. B. & Shimizu, N. (1990). Melting in the oceanic upper mantle: an ion microprobe study of diopsides in abyssal peridotites. *Journal of Geophysical Research* **95**(B3), 2661–2678.
- Katz, R. F., Spiegelman, M. & Holtzman, B. (2006). The dynamics of melt and shear localization in partially molten aggregates. *Nature* **442**, 676–679.
- Kelemen, P. B. (1990). Reaction between ultramafic rock and fractionating basaltic magma I. Phase relations, the origin of calc-alkaline magma series, and the formation of discordant dunite. *Journal of Petrology* **31**(1), 51–98.
- Kelemen, P. B., Shimizu, N. & Salters, V. J. M. (1995). Extraction of mid-ocean ridge basalt from the upwelling mantle by focused flow of melt in dunite channels. *Nature* **375**, 747–753.
- Kelemen, P. B., Hirth, G., Shimizu, N., Spiegelman, M. & Dick, H. J. (1997). A review of melt migration processes in the adiabatically upwelling mantle beneath oceanic spreading ridges. *Philosophical Transactions of the Royal Society of London* **355**(1723), 283–318.
- Keshav, S., Gudfinnsson, G. H., Sen, G. & Fei, Y. (2004). High-pressure melting experiments on garnet clinopyroxenite and the alkalic to tholeiitic transition in ocean-island basalts. *Earth and Planetary Science Letters* **223**(3–4), 365–379.
- Kogiso, T. & Hirschmann, M. M. (2006). Partial melting experiments of bimineraleclogite and the role of recycled mafic oceanic crust in the genesis of ocean island basalts. *Earth and Planetary Science Letters* **249**(3–4), 188–199.
- Kogiso, T., Hirschmann, M. M. & Frost, D. J. (2003). High-pressure partial melting of garnet pyroxenite: possible mafic lithologies in the source of ocean island basalts. *Earth and Planetary Science Letters* **216**(4), 603–617.
- Kogiso, T., Hirschmann, M. M. & Pertermann, M. (2004a). High-pressure partial melting of mafic lithologies in the mantle. *Journal of Petrology* **45**(12), 2407–2422.
- Kogiso, T., Hirschmann, M. M. & Reiners, P. W. (2004b). Length scales of mantle heterogeneities and their relationship to ocean island basalt geochemistry. *Geochimica et Cosmochimica Acta* **68**(2), 345–360.
- Kohlstedt, D. L. (1991). Structure, rheology and permeability of partially molten rocks at low melt fractions. In: Phipps Morgan, J., Blackman, D. K. & Sinton, J. M. (eds) *Mantle Flow and Melt Generation at Mid-ocean Ridges*. *American Geophysical Union, Geophysical Monographs* **71**, 103–121.
- Kornprobst, J. (1970). Les péridotites et les pyroxénolites du massif ultrabasique des Beni Bouchera: une étude expérimentale entre 1100 et 1550°C sous 15 à 30 kilobars de pression sèche. *Contributions to Mineralogy and Petrology* **29**, 290–309.
- Kumar, N., Reisberg, L. & Zindler, A. (1996). A major and trace element and strontium, neodymium, and osmium isotopic study of a thick pyroxenite layer from the Beni Bousera Ultramafic Complex of northern Morocco. *Geochimica et Cosmochimica Acta* **60**(8), 1429–1444.
- Kushiro, I. (1996). Partial melting of a fertile mantle peridotite at high pressures: an experimental study using aggregates of diamond. In: Basu, A. & Hart, S. (eds) *Earth Processes: Reading the Isotopic Code*. *American Geophysical Union, Geophysical Monographs* **95**, 109–122.
- Lambart, S., Laporte, D. & Schiano, P. (2009a). An experimental study of pyroxenite partial melts at 1 and 1.5 GPa: implications for the major-element composition of mid-ocean ridge basalts. *Earth and Planetary Science Letters* **288**, 335–347.
- Lambart, S., Laporte, D. & Schiano, P. (2009b). An experimental study of focused magma transport and basalt–peridotite interactions beneath mid-ocean ridges: implications for the generation of primitive MORB composition. *Contributions to Mineralogy and Petrology* **157**, 429–451.
- Langmuir, C. H., Klein, E. M. & Plank, T. (1992). Petrological systematics of mid-ocean ridge basalts: constraints on melt generation beneath ocean ridges. In: Phipps Morgan, J., Blackman, D. K. & Sinton, J. M. (eds) *Mantle Flow and Melt Generation at Mid-ocean Ridges*. *American Geophysical Union, Geophysical Monographs* **71**, 183–280.
- Laporte, D., Toplis, M., Seyler, M. & Devidal, J.-L. (2004). A new experimental technique for extracting liquids from peridotite at very low degrees of melting: application to partial melting of depleted peridotite. *Contributions to Mineralogy and Petrology* **146**(4), 463–484.
- Le Bas, M. J., Le Maitre, R. W., Streckeisen, A. & Zanettin, B. (1986). A chemical classification of volcanic rocks based on the total alkali–silica diagram. *Journal of Petrology* **27**, 745–750.
- Lenoir, X., Garrido, C. J., Bodinier, J.-L., Dautria, J.-M. & Gervilla, F. (2001). The recrystallization front of the Ronda peridotite: evidence for melting and thermal erosion of subcontinental lithospheric mantle beneath the Alboran Basin. *Journal of Petrology* **42**(1), 141–158.
- Le Roux, P. J., Le Roex, A. P. & Schilling, J.-G. (2002). MORB melting processes beneath the southern Mid-Atlantic Ridge (40–55°S): a role for mantle plume-derived pyroxenite. *Contributions to Mineralogy and Petrology* **144**, 206–229.
- Lundstrom, C. C., Gill, J. & Williams, Q. (2000). A geochemically consistent hypothesis for MORB generation. *Chemical Geology* **162**(2), 105–126.
- Luth, W. C. & Ingamells, C. O. (1965). Gel preparation of starting materials for hydrothermal experimentation. *American Mineralogist* **50**, 255–258.

- McKenzie, D. & O'Nions, R. K. (1991). Partial melt distributions from inversion of rare earth element concentrations. *Journal of Petrology* **32**(5), 1021–1091.
- Médard, E., Schmidt, M. W., Schiano, P. & Ottolini, L. (2006). Melting of amphibole-bearing wehrlites: an experimental study on the origin of ultra-calcic nepheline-normative melts. *Journal of Petrology* **47**(3), 481–504.
- Morgan, Z. & Liang, Y. (2003). An experimental and numerical study of the kinetics of harzburgite reactive dissolution with applications to dunite dike formation. *Earth and Planetary Science Letters* **214**(1–2), 59–74.
- Morgan, Z. & Liang, Y. (2005). An experimental study of the kinetics of lherzolite reactive dissolution with applications to melt channel formation. *Contributions to Mineralogy and Petrology* **150**(4), 369–385.
- O'Hara, M. J. (1968). Are ocean floor basalts primary magma? *Nature* **220**(5168), 683–686.
- Pearson, D. G., Davies, G. R. & Nixon, P. H. (1993). Geochemical constraints on the petrogenesis of diamond facies pyroxenites from the Beni Bousera peridotite massif, North Morocco. *Journal of Petrology* **34**(1), 125–172.
- Petermann, M. & Hirschmann, M. M. (2003). Partial melting experiments on a MORB-like pyroxenite between 2 and 3 GPa: Constraints on the presence of pyroxenite in basalt source regions from solidus location and melting rate. *Journal of Geophysical Research* **108**(B2), 2125, doi:10.1029/2000JB000118.
- Piccardo, G. B. & Vissers, R. L. M. (2007). The pre-oceanic evolution of the Erro-Tobbio peridotite (Voltri Massif, Ligurian Alps, Italy). *Journal of Geodynamics* **43**(4–5), 417–449.
- Pilet, S., Baker, M. B. & Stolper, E. M. (2008). Metasomatized lithosphere and the origin of alkaline lavas. *Science* **320**(5878), 916–919.
- Polvé, M. & Allègre, C. J. (1980). Orogenic lherzolite complexes studied by ^{87}Rb – ^{87}Sr : a clue to understand the mantle convection processes? *Earth and Planetary Science Letters* **51**, 71–93.
- Putirka, K. D. (1999). Clinopyroxene + liquid equilibrium to 100 kbar and 2450 K. *Contributions to Mineralogy and Petrology* **135**, 151–163.
- Putirka, K. D. (2008). Thermometers and barometers for volcanic systems. In: Putirka, K. D. & Tepley, F. J., III (eds) *Minerals, Inclusions and Volcanic Processes. Mineralogical Society of America and Geochemical Society, Reviews in Mineralogy and Geochemistry* **69**, 61–120.
- Putirka, K. D., Johnson, M., Kinzler, R. J. & Walker, D. (1996). Thermobarometry of mafic igneous rocks based on clinopyroxene–liquid equilibria, 0–30 kbar. *Contributions to Mineralogy and Petrology* **123**, 92–108.
- Putirka, K. D., Ryerson, F. J. & Mikaelian, H. (2003). New igneous thermobarometers for mafic and evolved lava compositions, based on clinopyroxene + liquid equilibria. *American Mineralogist* **88**, 1542–1554.
- Reisberg, L. C., Allègre, C. J. & Luck, J. M. (1991). The Re–Os systematic of Ronda ultramafic complex of southern Spain. *Earth and Planetary Science Letters* **105**, 196–213.
- Remaïdi, M. (1993). *Etude pétrologique et géochimique d'une association de péridotites réfractaires–pyroxénites dans le Massif de Ronda (Espagne)*. Ph.D. Thesis, Université de Montpellier II, 437 p.
- Rhodes, J. M., Dungan, M. A., Blanchard, D. P. & Long, P. E. (1979). Magma mixing at mid-ocean ridges: evidence from basalts drilled near 22°N on the Mid-Atlantic Ridge. *Tectonophysics* **55**, 35–61.
- Robinson, J. A. C., Wood, B. J. & Blundy, J. D. (1998). The beginning of melting of fertile and depleted peridotite at 15 GPa. *Earth and Planetary Science Letters* **155**(1–2), 97–111.
- Shervais, J. W., Wilshire, H. G. & Schwarzman, E. C. (1973). Garnet clinopyroxenite xenolith from Dish Hill, California. *Earth and Planetary Science Letters* **19**, 120–130.
- Sleep, N. H. (1984). Tapping of magmas from ubiquitous mantle heterogeneities: An alternative to mantle plumes. *Journal of Geophysical Research* **89**, 10029–10041.
- Sleep, N. H. (1988). Tapping of melts by veins and dykes. *Journal of Geophysical Research* **93**, 10255–10272.
- Smith, C. S. (1964). Some elementary principles of polycrystalline microstructure. *Metallurgical Reviews* **9**, 1–48.
- Smith, P. M. & Asimow, P. D. (2005). Adiaab1ph: A new public front-end to the MELTS, pMELTS, and pHMELTS models. *Geochemistry, Geophysics, Geosystems* **6**(1), doi:10.1029/2004GC000816.
- Sobolev, A. V., Hofmann, A. W., Kuzmin, D. V., Yaxley, G. M., Arndt, N. T., Chung, S.-L., Danyushevsky, L. V., Elliott, T., Frey, F. A., Garcia, M. O., Gurenko, A. A., Kamenetsky, V. S., Kerr, A. C., Krivolutsкая, N. A., Matvienkov, V. V., Nikogosian, I. K., Rocholl, A., Sigurdsson, I. A., Sushchevskaya, N. M. & Teklay, M. (2007). The amount of recycled crust in sources of mantle-derived melts. *Science* **316**(5823), 412–417.
- Sparks, D. W. & Parmentier, E. M. (1991). Melt extraction from the mantle beneath spreading centers. *Earth and Planetary Science Letters* **105**(4), 368–377.
- Spiegelman, M., Kelemen, P. B. & Aharonov, E. (2001). Causes and consequences of flow organization during melt transport: The reaction infiltration instability in compactible media. *Journal of Geophysical Research* **106**(B2), 2061–2077.
- Stolper, E. M. (1980). A phase diagram for mid-ocean ridge basalts: Preliminary results and implications for petrogenesis. *Contributions to Mineralogy and Petrology* **74**(1), 13–27.
- Takahashi, N. (1992). Evidence for melt segregation towards fractures in the Horoman mantle peridotite complex. *Nature* **359**(6390), 52–55.
- Tommasi, A., Godard, M., Coromina, G., Dautria, J.-M. & Barszczus, H. (2004). Seismic anisotropy and compositionally induced velocity anomalies in the lithosphere above mantle plumes: a petrological and microstructural study of mantle xenoliths from French Polynesia. *Earth and Planetary Science Letters* **227**(3–4), 539–556.
- Toplis, M. J. (2005). The thermodynamics of iron and magnesium partitioning between olivine and liquid: criteria for assessing and predicting equilibrium in natural and experimental systems. *Contributions to Mineralogy and Petrology* **149**(1), 22–39.
- Van der Wal, D. & Bodinier, J. L. (1996). Origin of the recrystallisation front in the Ronda peridotite by km-scale pervasive porous melt flow. *Contributions to Mineralogy and Petrology* **122**, 387–405.
- Wark, D. A., Williams, C. A., Watson, E. B. & Price, J. D. (2003). Reassessment of pore shapes in microstructurally equilibrated rocks, with implications for permeability of the upper mantle. *Journal of Geophysical Research* **108**(B1), 2050, doi:10.1029/2001JB001575.
- Wasylenki, L. E., Baker, M. B., Kent, A. J. R. & Stolper, E. M. (2003). Near-solidus melting of the shallow upper mantle: partial melting experiments on depleted peridotite. *Journal of Petrology* **44**(7), 1163–1191.
- Yaxley, G. & Green, D. H. (1998). Reactions between eclogite and peridotite: mantle refertilisation by subduction of oceanic crust. *Schweizerische Mineralogische und Petrographische Mitteilungen* **78**(2), 243–255.